1 **Near real-time atmospheric and oceanic science products of Himawari-8/9**

2 **geostationary satellites over the South China Sea**

3

4 Jian Liu[1], Jingjing Yu[1], Chuyong Lin[1], Min He[1], Haiyan Liu[1], Wei Wang[2], Min Min[2]*

5

6

7 [1] School of Geography and Ocean Science, Ministry of Education Key Laboratory for Coast

8 and Island Development, Nanjing University, Nanjing 210023, China, and Southern Marine

9 Science and Engineering Guangdong Laboratory (Zhuhai), Zhuhai 519082, China

10 [2] School of Atmospheric Sciences and Guangdong Province Key Laboratory for Climate

11 Change and Natural Disaster Studies, Sun Yat-sen University, Zhuhai 519082, China

12

13

14

15

16

17

18 *Corresponding author: minm5@mail.sysu.edu.cn

19

20

21

22

23

24

25

26

Abstract

The initial release of near real-time (NRT) atmospheric and oceanic science products from Japanese Himawari-8/9 (H8/9) geostationary (GEO) satellites over the South China Sea (SCS) was unveiled in 2024. The primary objective behind crafting these NRT H8/9 satellite products is to facilitate weather and marine environment monitoring, enhance maritime security, and aid ocean navigation, among other purposes. As part of this investigation, a novel NRT data processing system was devised to generate a variety of regional H8/9 GEO satellite science products within a resolution of 10 minutes and a gridded resolution of $0.05° × 0.05°$ from November 3, 2022 to the present. This algorithm system was built upon the preceding FengYun (FY) geostationary satellite algorithm testbed (FYGAT), which was the prototype of FY-4 GEO meteorological satellite science product operational processing system. These regional H8/9 GEO satellite science products encompass a range of crucial data such as cloud mask, fraction, height, phase, optical and microphysical properties, layered precipitable water, sea surface temperature, etc. We subjected these products to rigorous evaluations against high-quality analogous satellite products and reanalysis data spanning one year in 2023. The validations underscore a strong consistency between the H8/9 GEO satellite atmospheric and oceanic science products over the SCS and the referenced products. Nevertheless, slight discrepancies in these satellite science products were identified, primarily stemming from variations in sensor/dataset characteristics, retrieval algorithms, and geometric conditions. These outcomes demonstrate the suitability of the first edition of NRT atmospheric and oceanic science products of H8/9 satellites over the SCS in supporting the intended quantitative applications. This NRT GEO satellite data record is publicly accessible through the File Transfer Protocol (FTP) provided by the Southern Marine Science and Engineering Guangdong Laboratory (Zhuhai) in China. Free access to the dataset can be found at https://doi.org/10.6084/m9.figshare.25015853 (Liu Jian, 2024).

Keywords: Cloud; Geostationary Satellite; South China Sea; Layered Precipitable Water; Sea surface temperature.

1 Introduction

The South China Sea is located to the south of mainland China and in the western Pacific Ocean. It stands as the largest and deepest sea area in China, with an average depth of 1212 meters and reaching a maximum depth of 5559 meters. Due to its proximity to the equator, the SCS receives a substantial amount of solar radiation, resulting in high local temperatures and humidity. The regional annual average air temperature ranges from 298.15 K to 301.15 K. Even during the coldest months, the average temperatures remain above 293.15 K, while extreme high-temperature events can reach about 306.15 K. The average sea surface temperature (SST) in the SCS is around 299.15 K, and the seasonal variation is not significant. Furthermore, the South China Sea and the Western Pacific serve as abundant sources of water vapor, leading to considerable precipitation in the SCS. Typhoon-related rainfall accounts for about one-third of the total rainfall in the region. On average, the SCS experiences over 1300 mm of rainfall annually, with the majority concentrated in the summer half-year (Wang et al., 2011; Wang et al., 2009; Ding and Liu, 2001).

The SCS region experiences a distinct tropical maritime monsoon climate. Beginning in October each year, winter air currents originating from Siberia and the Mongolian Plateau consistently flow toward the SCS (Martin and Howland, 1982). As a result, from November to March of the following year, the SCS region is dominated by the northeast monsoon. Starting in April, the SCS is influenced by tropical and equatorial ocean air masses, inducing the prevalence of the southwest monsoon from May to September. Additionally, the SCS is often affected by typhoons during the summer and autumn seasons. About 70% of these typhoons originate from the Western Pacific, east of the Philippines, and the vicinity of the Caroline Islands, while the remaining 30% are generated locally in the sea areas near the Xisha and Zhongsha Islands in the SCS (Ding and Liu, 2001; Wang et al., 2020; Niu and Feng, 2021; Jiang et al., 2023).

Due to the lack of ground-based observations over the SCS, satellites, particularly geostationary (GEO) meteorological satellites, have become the most effective means of observing weather patterns, climate, and environmental changes in oceanic regions. For instance, satellite-based rain rate, SST, outgoing longwave radiation (ORL), and convective clouds, etc. are commonly used to identify the summer monsoon, marine heatwave, rainfall, and convection over the SCS (Liu et al., 2014; Xu et al., 2021; Li et al., 2022b; Koseki et al., 2013; Zhou et al., 2024). In recent years, countries across the

91   world, such as China, U.S., Japan, and Korea, have made their own remarkable progress

92   in the development of next-generation geostationary meteorological satellites.

93   Enhanced imaging capabilities in spectral, temporal, and spatial resolutions of the next-

94   generation GEO meteorological satellite allows for more detailed and accurate

95   observations of cloud formations, atmospheric conditions, and natural disasters like

96   hurricanes and typhoons, such as Fengyun-4A/B (FY-4) operated by the China

97   Meteorological Administration (CMA) and Himawari-8/9 (H8/9) satellites operated by

98   the Japan Meteorological Agency (JMA) (Yang et al., 2017; Schmit et al., 2017; Husi

99   et al., 2019; Kim et al., 2021). In additional to GEO advanced imager, many nations

100 have equipped their geostationary lightning and infrared hyperspectral sounding

101 detection sensors to track and analyze thunderstorms, lightning activities, atmospheric

102 temperature and humidity profiles, and even wind fields in real-time (Min et al., 2017b;

103 Ma et al., 2021; Li et al., 2022a).

104   Although the JAXA (Japan Aerospace Exploration Agency) official FTP site

105 (ftp.ptree.jaxa.jp) has already offered the freely download links for some H8/9 Level-2

106 (L2) science products, such as cloud phase and optical depth (Husi et al., 2019), from

107 July 7 of 2015, to the present with approximate two hours lag, the relatively low

108 timeliness and lack of variety of operational satellite science products have seriously

109 affected the data quantitative applications in weather and marine environment

110 monitoring over the SCS. Particularly, time-delayed GEO satellite products cannot be

111 utilized in maritime security and navigation fields, which are of vital importance as it

112 ensures the safety of crew members, transportation of goods, protection of the marine

113 environment, etc. (Soldi et al., 2021). However, as recommended by the JMA, the near

114 real-time down-sampling full-disk H8/9 Level-1B (L1B) radiance data (including 14

115 bands with horizontal resolutions of 1 km (visible, VIS) and 4 km (near infrared and

116 infrared, NIR and IR bands), and excluding two VIS bands at 0.47 μm and 0.51 μm)

117 are able to be received by using the compact and exclusive geostationary satellite data

118 receiving antenna from the JMA Himawari-Cast (Xia et al., 2023; Wang et al., 2019).

119 Therefore, based on the received real-time H8/9 full-disk L1B data, the primary goal of

120 this investigation is to develop several NRT L2 Atmospheric aNd Oceanic science

121 products over the SCS (abbreviated as NANO_SCS) that are released online. It is the

122 first edition of the NRT H8/9 GEO satellite science products generated by the

123 NANO_SCS system. The next sections will be devoted to the introduction and

124 validation of these NRT H8/9 GEO satellite scientific products. Both the NANO_SCS

125 satellite data processing and management systems are operated by the Southern Marine
126 Science and Engineering Guangdong Laboratory (Zhuhai) of China.

127   The subsequent sections of this study are meticulously organized as follows.
128 Section 2 briefly introduces the Himawari-8/9 satellites, elucidating the intricate details
129 of the main processing or production flow, as well as shedding light on the remarkable
130 NRT science products specifically tailored for the South China Sea region. Section 3
131 shows some sample results and verification of key science products in terms of
132 accuracy and reliability. Section 4 elucidates data download method. Finally, in Section
133 5, we summarize the main conclusions of this study, while also outlining our future
134 vision plans for further enhancing and expanding the scope of the NANO_SCS dataset.
135

136 **2 Data production**

137 *2.1 Data*

138   The Himawari-8/9 satellites, which are the new-generation and state-of-the-art GEO
139 meteorological satellites operated by the JMA, were successfully launched on October
140 7, 2014, and November 2, 2016, respectively. These advanced satellites operate in a
141 highly sophisticated three-axis stabilized mode, ensuring high spatial-temporal, precise
142 and stable observations. It is worth highlighting that on December 13, 2022, at 05:00
143 UTC, the H9 GEO meteorological satellite seamlessly replaced its predecessor, the H8
144 GEO satellite, marking a significant milestone in GEO satellite operations
145 (https://www.data.jma.go.jp/mscweb/en/index.html). This strategic location allows for
146 comprehensive full-disk observation mode, enabling the satellites to capture detailed
147 imagery of the entire Earth's disk, with a particular focus on the Japanese island and its
148 surrounding areas. The Advanced Himawari Imager (AHI), as a unique and highly
149 advanced optical sensor designed specifically for earth viewing, has 16 independent
150 earth-view bands, covering an extensive range of wavelengths from 0.45 to 13.3 μm.
151 These bands include three visible (VIS) bands, three near-infrared (NIR) bands, and ten
152 infrared (IR) bands, each serving a specific purpose in capturing and analyzing various
153 aspects of the Earth's atmosphere and surface. The AHI routinely operates in two
154 observation modes: a full-disk observation mode that captures full disk images within
155 a 10-minute time interval, and a fast regional scanning mode that allows for swift
156 maneuvering and scanning within a 2.5-minute interval. This regional scanning mode
157 is particularly useful for capturing high-resolution imagery of specific regions of

interest, enabling detailed analysis and examination of localized weather events. The nominal spatial resolutions of the H8/9-AHI sensor vary depending on the specific band being utilized. For the VIS band at 0.65 μm, the spatial resolution is 0.5 km. The NIR bands have a spatial resolution of 1 km, while the IR bands have a spatial resolution of 2 km (Husi et al., 2019; Bessho et al., 2016; Letu et al., 2020; Min et al., 2019). In this study, we only used the down-sampling H8/9 L1B radiance data mentioned before to produce NRT dataset. The spatial resolution for the down-sampling VIS band at 0.65 μm was reduced to 1.0 km, while the other bands were down-sampled to 4.0 km. The scope of this investigation covers the South China Sea region, specifically from 0° to 40°N latitude and 100°E to 140°E longitude. The utilization of IR bands with a spatial resolution of 4.0 km limits the related L2 satellite science products to the same resolution. Therefore, based on the products with the spatial resolution of 4.0 km, the final regional L2 atmospheric and oceanic science products are analyzed and projected into a user-friendly gridded resolution of 0.05° × 0.05°.

The NRT GEO satellite retrieval system (or NANO_SCS system) developed in this study also utilizes the high-resolution operational numerical weather prediction (NWP) data from Global Forecast System (GFS) as ancillary data, which has a gridded horizontal resolution of 0.25° × 0.25° and encompasses a 41 vertical layers ranging from 1000 to 0.01 hPa within a 3-hour time interval. The GFS NWP data can be effortlessly accessed and downloaded from the National Oceanic and Atmospheric Administration (NOAA) website (https://nomads.ncep.noaa.gov/pub/data/nccf/com/gfs/prod) at four distinct initial forecast times (00_00, 06_00, 12_00, and 18_00 UTC). To ensure optimal efficiency for the operations of subsequent day, only 9 continuous data (ranging from 018, 021, 024, ... to 042) generated at a fixed initial forecast time of UTC 06_00 are selectively downloaded within a predefined time period each day (Whitaker et al., 2008).

We collect and use one year (2023) of Climate Data Records (CDR) from the latest MODIS (Moderate Resolution Imaging Spectroradiometer) Collection-6.1 Level-2 cloud, land surface temperature (LST), and sea surface temperature (SST) products to validate the NRT H8/9 GEO satellite science products (Platnick et al., 2003; Platnick et al., 2017). MODIS, as a key optical sensor aboard NASA's Terra and Aqua polar-orbiting satellites since 1999 and 2002 (respectively), can provide high resolution (1.0 km) L2 science products about the Earth's surface and atmosphere (https://search.earthdata.nasa.gov/search). MODIS data are freely available to the

192   public and are widely used by scientists, government agencies, and researchers around

193   the world, which are often used to verify the other congeneric satellite products (Min

194   et al., 2020). Furthermore, we also compare the NRT layered precipitable water (LPW)

195   product over the SCS with matched ERA5 reanalysis data (the fifth-generation

196   European Center for Medium Range Weather Forecasts Reanalysis data) (Hersbach et

197   al., 2020). The hourly layered specific humidity data for the same year (2023) with a

198   horizontal resolution of 0.25°×0.25° have been downloaded freely from the ERA5

199   dataset. This data will be employed for the validation of the layered precipitable water

200   product of H8/9 GEO satellite. You can access the data at

201   https://cds.climate.copernicus.eu/cdsapp#!/home.

202

203   *2.2 NRT processing flow and science products*

204   As extensively discussed in the former study by (Min et al., 2017b), significant strides

205   were made in the development of the operational prototypes of FY-4 GEO satellite

206   science product algorithms. These remarkable advancements were achieved through

207   the collaborative efforts of the scientists in the FY-4 GEO satellite Algorithm Working

208   Group (AWG) in China, who successfully developed two highly robust Fengyun

209   science product algorithm testbeds (or FYGAT) specifically tailored for imagers and

210   sounders. For a comprehensive understanding of the intricate details of FYGAT,

211   interested readers are strongly encouraged to refer to the aforementioned literature

212   written by (Min et al., 2017b). The FYGAT for imager is the key module of the

213   NANO_SCS system for rapidly retrieving the first edition of NRT L2 science products

214   of H8/9 GEO satellites.

215   Figure 1 shows the comprehensive NRT processing flowchart of the NANO_SCS

216   system. The dark gray shading cylinder icons in the figure represent the key processing

217   modules of the system, including retrieval, projection, and drawing modules. Following

218   the synthesis of NRT satellite data, the retrieval module initially retrieves the cloud

219   mask product to identify clear and cloudy-sky pixels within the targeted SCS region.

220   Then, for cloudy-sky pixels, he retrieval module sequentially executes algorithms for

221   retrieving cloud fraction, cloud type/phase, cloud top properties, cloud optical and

222   microphysical properties, and cloud base properties products. However. the accurate

223   retrieval of science products from previous algorithms is crucial for the successful

224   execution of subsequent backend algorithms. For instance, the cloud optical and

225   microphysical properties algorithm relies on inputs such as cloud phase and top

226 properties to determine specific ice/water cloud optical and radiative properties lookup
227 tables (LUT) and atmospheric correction methods above the cloud (Platnick et al., 2017;
228 Walther et al., 2011) used in retrieval procedure. In a stark contrast, other science
229 algorithms for clear-sky pixels can be executed in parallel as they are independent of
230 each other, such as the algorithms for land surface temperature (LST) and sea surface
231 temperature (SST). It is important to note that due to retrieval efficiency and computing
232 resource limitations, the physics-based layered precipitable water (LPW) algorithm
233 (Zhu et al., 2023) is executed only once every half an hour.

234　　Table 1 provides a list of the main NRT H8/9 GEO satellite atmospheric and oceanic
235 science products in the first edition, along with their corresponding variables, generated
236 by the NANO_SCS system from 3 November 2022 to the present. It includes the
237 variable name, valid value, and corresponding notes of satellite science products. These
238 products are stored in the Hierarchical Data Format-5 (HDF5) format within a 10-
239 minute interval. The NRT GEO satellite science product is typically referred to as
240 "AHI9_L2_CLM_20230815_0650_4000M_proj.hdf5". In this naming convention, the
241 abbreviation of "CLM" stands for Cloud Mask (all abbreviations are three characters
242 long), while "20230815_0650" denotes the specific observation time of the satellite
243 data, including year, month, day, hour, and minute. Lastly, "4000M_proj" indicates the
244 spatial resolution of 4000 meters and projected data. Certain related variables, such as
245 cloud top temperature, pressure, and height, are stored in the same HDF5 format GEO
246 satellite science product file, specifically the CTP (Cloud Top Properties) product file
247 (refer to Table 1).

248　　Figure 2 displays the quick view images of cloud top height, cloud mask, cloud base
249 height, and cloud optical depth at 03:00 UTC on July 31, 2023, as well as atmospheric
250 total precipitable water (from LPW product) and SST retrieved at clear-sky pixels at
251 10:00 UTC on August 15, 2023, over the SCS. These NRT product images are obtained
252 from the NANO_SCS system. The four cloud product subfigures from July 31, 2023,
253 capture the presence of Super Typhoon "Khanun" (its international number: 2306),
254 which originated in the southwestern waters of Guam on July 22, 2023. It has been
255 observed that the cloud system of Super Typhoon "Khanun" can reach maximum cloud
256 top heights exceeding 16 km and minimum cloud base height lower than 1 km. The
257 productions of all the NRT satellite science products and quick view images of the
258 NANO_SCS system are typically delayed by approximately 17 minutes from the
259 observation time. Besides, a user-friendly quick-view website

260 (http://meteorsatellite.hellosea.org.cn/#/index) has been created to provide users with a

261 convenient way to access and monitor the NRT H8/9 satellite data over the SCS.

262

263 **3. Results and validations**

264 *3.1 Cloud mask and fraction*

265   To differentiate between clear-sky and cloudy pixels in satellite earth-view image,

266 the cloud mask (CLM) product is firstly retrieved by the NANO_SCS system (refer to

267 Figure 1). This serves as a fundamental and primary L2 scientific output of GEO

268 satellite imaging sensors, playing a crucial role in generating high-quality subsequent

269 satellite products. As mentioned in the previous studies (Liang et al., 2023; Wang et al.,

270 2019; Heidinger et al., 2012), we used the new unified cloud mask algorithm (Wang et

271 al., 2019) of early development to retrieve and generate H8/9 CLM product firstly.

272 Utilizing the 0.64, 1.61, 3.88, 7.3, 11.2, and 12.3 μm channels of H8/9-AHI, the CLM

273 algorithm on this GEO satellite will perform 13 distinct cloud/clear-sky tests. These

274 tests are categorized into four groups: solar reflectance (SolRef), infrared (IR),

275 shortwave infrared (SWIR), and spatial uniformity tests (Wang et al., 2019; Xia et al.,

276 2024).

277   After successfully retrieving the cloud mask product, similar to the MODIS

278 algorithm (Zhao and Girolamo, 2006), cloud fraction (CLF) is calculated in a down-

279 sampled 5×5 neighboring pixel box as follows:

280 *Cloud Fraction* $= 100\% \times (A + B)/(5 \times 5)$,   (1)

281 where A and B represent the total numbers of cloudy and probably cloudy pixels in the

282 same 5×5 neighboring pixel box, respectively. It is noting that the cloud fraction

283 product is also projected into a user-friendly gridded resolution of 0.05° × 0.05°. More

284 descriptions on these two products can be found in Table 1.

285   A pixel-to-pixel validation was performed on the H8/9 satellite CLM product over

286 the SCS using one year of MODIS data from the NANO_SCS system. To quantitatively

287 assess the quality of the GEO satellite CLM product, we employed four significant

288 scores: the probability of detection (POD) or recall rate, the false-alarm ratio (FAR),

289 the hit rate (HR) or accuracy, and the Kuiper's skill score (KSS). These metrics were

290 divided into PODcld, PODclr, FARcld, and FARclr, indicating clear and cloudy pixels

291 respectively. For detailed equations and meanings, please refer to previous literature

292 (Wang et al., 2019). In Figure 3a~3d, we present two cloud mask comparison samples

293 between H9/AHI GEO satellite and MODIS at 05:10 and 17:20 UTC on January 8,

294   2023. It is evident that the CLM results from H9/AHI align well with the latest MODIS

295   official products across both land and sea. Additionally, Figure 3e displays the POD,

296   FAR, HR, and KSS scores of H9/AHI results for all matched pixels over land and ocean.

297   Notably, both PODcld and HR exceed 0.90, consistent with our prior study (Wang et

298   al., 2019), indicating a relatively high-quality CLM product. Moreover, considering

299   that cloud fraction depends on the cloud mask product (refer to Eq. (1)), we opted

300   against using similar products for verification in this analysis.

301

302   *3.2 Cloud type and phase*

303   Cloud type and phase as thermodynamics characteristics signify the state of water

304   vapor and minuscule particles within the cloud. It plays a critical role in weather and

305   climate research as different cloud phases influence the reflection and absorption of

306   solar radiation, consequently impacting Earth's energy balance and climate change

307   (Mülmenstädt et al., 2021). Due to the similarities in detection channels (using 7.3, 8.5,

308   11.2, and 12.3 μm channels), the cloud type and phase (CLP) retrieval algorithm

309   developed here for H8/9-AHI was based on the corresponding algorithm used for U.S.

310   new-generation Geostationary Operational Environmental Satellites (GOES-R)

311   (Pavolonis et al., 2005; Pavolonis, 2010b). The physical foundation of this algorithm is

312   the radiative transfer equation or forward model for cloudy-sky at a specific infrared

313   wavelength λ, which can be expressed as follows (Min et al., 2020):

314   $I_{obs}(\lambda) = \varepsilon(\lambda)I_{ac}(\lambda) + \varepsilon(\lambda)T_{ac}(\lambda)B(\lambda, t_{eff}) + I_{clr}(\lambda)[1 - \varepsilon(\lambda)],$ (2)

315   where I_{obs} is the observed radiance, I_{clr} is the clear-sky radiance, and I_{ac} is the above-

316   cloud upwelling atmospheric radiance, respectively. I_{clr} can be precisely simulated by

317   the coupled fast IR radiative transfer model in the FYGAT system with the input of

318   matched GFS NWP data. ε and T_{ac} respectively represent the cloud emissivity and

319   above-cloud transmittance. B and t_{eff} are the Planck function and the cloud effective

320   temperature, respectively.

321   From Eq. (2), a pair of effective cloud emissivity from two different channels can be

322   used to calculate the ratio of effective absorption optical thickness τ_{abs} of cloud, which

323   is known as the beta ratio (β) and written as follows (Heidinger and Pavolonis, 2009;

324   Parol et al., 1991):

325   $\beta_{obs} = \frac{\ln[1-\varepsilon(\lambda_1)]}{\ln[1-\varepsilon(\lambda_2)]} = \frac{\tau_{abs}(\lambda_1)}{\tau_{abs}(\lambda_2)},$ (3)

326　Actually, this parameter represents the ratio of the effective absorption optical depth at

327　two different channels or wavelengths. It can describe β_{obs} by utilizing the computed

328　single scattering properties of cloud particles, along with a given cloud particle size

329　distribution and optical properties. (Parol et al., 1991). The β_{theory} can be expressed as

330　follows:

331　$$\beta_{theory} = \frac{[1-\omega(\lambda_1)g(\lambda_1)]\alpha_{ext}(\lambda_1)}{[1-\omega(\lambda_2)g(\lambda_2)]\alpha_{ext}(\lambda_2)}, \tag{4}$$

332　where ω, g, and α_{ext} are the single scattering albedo, asymmetry parameter, and

333　extinction cross section, respectively. Considering the weak impact of multiple

334　scattering, Parol et al., (1991) demonstrated a good approximation of $\beta_{theory} \approx \beta_{obs}$ in the

335　range of 8~15 μm. Eq. (4) is independent of satellite observed radiance, cloud altitude,

336　or cloud optical thickness. By using β ratio instead of brightness temperature difference

337　(BTD), it not only considers the contribution of clear-sky conditions to radiation but

338　also provides a method to link observations with theoretical cloud particle distribution

339　and optical properties.

340　　Based on the differences in β ratios (i.e. β[8.5/11.2μm], β[12.3/11.2μm], and

341　β[7.3/11.2μm]) between ice and water clouds, this algorithm effectively identifies cloud

342　type and phase by integrating cloud emissivity ε with observed brightness temperature.

343　More details of this algorithm can be found from the previous literatures (Pavolonis,

344　2010a; Pavolonis, 2010b). The six specific cloud types of this CLP product include

345　liquid water (cloud top temperature>273K), supercooled water (liquid water clouds

346　with cloud top temperature<273K), mixed (which encompass both ice and water

347　clouds), optically thick ice, optically thin ice, and multilayered ice clouds. The cloud

348　phase product can be defined by summarizing the first three types of clouds and ice

349　phase clouds using the last three different ice clouds (see Table 1).

350　　Figure 4 illustrates the cloud phase comparisons between the H9/AHI GEO satellite

351　and MODIS at 05:10 UTC on January 8, 2023, and 04:30 UTC on July 10, 2023. This

352　comparison reveals consistent results between the two products. Notably, in Figures 4a

353　and 4c, the new H9/AHI cloud phase product identifies some newly added mixed-phase

354　cloud targets, a feature lacking in the MODIS official cloud phase product (King et al.,

355　1997). However, despite this addition, the distribution pattern of cloud phases remains

356　consistent between the two products as depicted in Figure 4. The POD and FAR for ice

357　and water clouds (Lai et al., 2019) are 0.94/0.17 and 0.68/0.14, respectively.

358

359 *3.3 Cloud top and base properties*

360   Cloud geometry thickness (CGT), including top and base heights (CTP and CBP),

361 enables the profiling of the vertical structure of clouds, which is vital for understanding

362 global weather and climate systems (Viúdez-Mora et al., 2015; Wang et al., 2022).

363 Using the same beta ratio (β) theory discussed in Section 3.2, the optimal estimation

364 (OE) method (Rodgers, 2000), and observed brightness temperatures (BT) at 11.2, 12.3,

365 and 13.3 μm channels, a classical one-dimensional variational (1DVAR) algorithm

366 applies a cost function ζ (refer to Eq. 5) to estimate the cloud top temperature (CTT),

367 which can be written as follows :

368 $$\zeta = [x - x_a]^T Cov_a^{-1}[x - x_a] + [y - M(x)]^T Cov_y^{-1}[y - M(x)], \qquad (5)$$

369 where x, y, x_a, $M(x)$, Cov_a, and Cov_y, represent the posterior state vectors, the

370 observation vectors (include $BT_{11\mu m}$, $BTD_{11\text{-}12\mu m}$, and $BTD_{11\text{-}13.3\mu m}$), the priori state or

371 first guessed vectors (include CTT, cloud emissivity ε at 11μm, and $\beta[12/11\mu m]$), the

372 forward radiative transfer model (based on Eq. (2) in the CLP retrieval algorithm), and

373 the error covariance matrices of the priori state vectors (x_a) and the differences between

374 observations and the forward radiative transfer model of $M(x)$, respectively. As a

375 nonlinear least squares fitting problem, the classical Levenberg-Marquardt iteration

376 method is used here to minimize the cost function of ζ, which can be written as follows

377 (Levenberg, 1944):

378 $$\delta x = \left(Cov_a^{-1} + K^T Cov_y^{-1}K\right)^{-1}\left(K^T\left(Cov_y^{-1}[y - M(x)]\right) + Cov_a^{-1}[x_a - x]\right), \qquad (6)$$

379 where K signifies the Jacobi or Kernel matrix. The optimal values of CTT, cloud

380 emissivity, and $\beta[12/11\mu m]$ will be obtained when the iteration converges the satellite

381 observation vectors of y. It is worth noting that the beta ratio (β) plays a specific role in

382 this retrieval algorithm by analytically solving equations in the Jacobi matrix stated in

383 Eq. (6), thereby resulting in a significant enhancement of operational processing

384 efficiency. After obtaining the optimal CTT, the matched GFS-NWP temperature

385 profile is utilized to interpolate the corresponding cloud top height and pressure. For

386 more detailed information on the CTP retrieval algorithm of H8/9-AHI, please refer to

387 the study from Min et al., 2020.

388   In contrast, the successful retrieval of cloud base properties requires more inputs such

389 as cloud mask, type, top height, and optical and microphysical properties (convert to

390 cloud water path, CWP, unit = g/m^2) as discussed in Sections 3.1, 3.2, and 3.4. Wang

391 et al. (2023) have recently developed and improved a new CBP retrieval algorithm for

GEO H8/9-AHI, which refers to the CLAVR-x cloud base properties algorithm (Clouds from AVHRR Extended, NOAA's operational cloud processing system for the AVHRR) (Wang et al., 2024; Noh et al., 2017). This algorithm can only be executed during the daytime (solar zenith angle < 65°) because it relies on cloud top height (CTH) and cloud water path to calculate the two linear fitting coefficients, namely slope (A_1) and intercept (A_2) (Noh et al., 2017). These two coefficients are determined through piecewise fitting using the CTH, CWP, and cloud base height (CBH) data obtained from the joint CloudSat/CALIPSO (Cloud-Aerosol Lidar and Infrared Pathfinder Satellite Observation) product (Noh et al., 2017). Once the two corresponding fitting coefficients are obtained, the cloud geometric thickness can be calculated as follows:

$$CGT = A_1 \times CWP + A_2, \tag{7}$$

After that, the CBH can be easily calculated using the formula CBH = CTH − CGT.

Previous studies have validated the CTH and CBH products obtained through the same algorithms used for the H8 satellite, leveraging joint CloudSat/CALIPSO product (Wang et al., 2024; Wang et al., 2022; Min et al., 2020; Min et al., 2017b). The mean absolute error (MAE) and standard deviation (STD) for GEO satellite CTH are reported as 3.18 km and 3.75 km, respectively, with a noticeable increase associated with higher CTH values. Additionally, the MAE and root-mean-square error (RMSE) for CBH, retrieved by the same GEO CLAVR-x algorithm, stand at 1.938 km and 2.91 km, as reported in prior studies (Wang et al., 2024; Min et al., 2020). In Figure 5, CTH comparisons between the H9/AHI GEO satellite and MODIS are presented for 18:50 UTC on October 8, 2023, and 04:30 UTC on July 10, 2023. The figure well demonstrates consistent CTH values and horizontal distributions derived from both H9/AHI and MODIS datasets.

3.4 Cloud optical and microphysical properties

The cloud optical thickness (COT or τ_{cld}) and particle effective radius (CER or r_{cld}, unit=μm) (or cloud optical and microphysical properties) primarily characterizes the radiative properties of clouds, highlighting their influence on the equilibrium of Earth's radiation budget (Platnick et al., 2017). These two parameters are commonly used in a general circulation model (GCM) to define cloud parameterization schemes for climate modeling (Chou et al., 1998). The cloud optical and microphysical properties algorithm during the daytime (solar zenith angle < 65°) utilizes the reflected solar radiation measured by a non-absorbing channel (0.64 μm) to retrieve cloud optical thickness (τ_{cld}).

426   Additionally, it uses the reflected solar radiation measured by an absorbing channel

427   (2.23 μm) to retrieve cloud particle effective radius (r_{cld}) (Walther et al., 2011). The

428   fundamental physical principle of this algorithm is to leverage the sensitivities of the

429   non-absorbing and absorbing channels to cloud optical thickness (τ_{cld}) and cloud

430   particle effective radius (r_{cld}) in the atmospheric radiative transfer process, as

431   demonstrated by a previous study (Nakajima and King, 1990).

432   The water and ice cloud optical and radiative properties look-up tables (LUT) with a

433   modified Gamma size distribution for fast retrieval were built based on spherical

434   particle with the scattering properties given by the Mie theory and MODIS Collection-

435   6 severely roughened aggregated columns ice crystal (Min et al., 2017a; Platnick et al.,

436   2017; Baum et al., 2007), respectively. By utilizing the similar 1DVAR algorithm

437   discussed in Section 3.3, along with water/ice cloud LUTs, observed reflectance at 0.64

438   and 2.23 μm channels, and additional ancillary data, the optimal cloud optical thickness

439   (τ_{cld}) and cloud particle effective radius (r_{cld}) can be iteratively calculated using the OE

440   algorithm (Walther et al., 2011). Differing from Equation (2), the variables or first-

441   order partial derivative from forward cloud reflectance model in the Jacobi matrix are

442   derived from a formula for solar reflectance observed by satellite, which can be written

443   as follows (Nakajima and King, 1990):

444    $$R_{obs} = R_{cld} + \frac{A_s}{1-A_s R'_{cld}} T_{cld} T'_{cld}, \tag{8}$$

445   where R_{obs} is the total cloud bidirectional reflectance function at the top of the

446   atmosphere (TOA). A_s is the albedo at the Lambertian surface of a uniform single-

447   layer cloud. R_{cld} and T_{cld} signify the cloud reflectance and downward transmittance

448   (diffuse and direct), respectively. R'_{cld} and T'_{cld} are the cloud spherical albedo and the

449   transmittance below the cloud, respectively. After retrieving τ_{cld} and r_{cld}, ice and liquid

450   cloud water paths (IWP/LWP) are calculated using empirical formulas (Bennartz, 2007;

451   Heymsfield et al., 2007), which are expressed as follows:

452    $$LWP = \frac{5}{9} \tau_{cld} r_{cld} \rho, \tag{9}$$

453    $$IWP = \frac{\tau_{cld}^{1/0.84}}{0.065}, \tag{10}$$

454   where ρ is the density of liquid water (=1.0 g/cm^3).

455   Figure 6 shows the cloud optical depth and effective radius comparisons between the

456   H9/AHI GEO satellite and MODIS (Platnick et al., 2017) at 05:40 UTC on October 30,

457   2023. We find consistent retrieval results between these two different COT and CER

458 products. Besides, Figures 6e and 6f respectively show the comparisons of the one year

459 COT and CER from MODIS and H9/AHI data over the SCS with the related scores,

460 such as MAE, MBE, R and RMSE. The differences are likely to be attributed to the

461 different spatial resolutions and retrieval algorithms used between these two satellite

462 products (Letu et al., 2019; Wang et al., 2024).

463

464 *3.5 Layered precipitable water and atmospheric instability indices*

465 The atmospheric temperature and humidity profiles provide valuable information

466 about the vertical distribution of water vapor and temperature at various altitudes. This

467 is very crucial for studying cloud formation, precipitation patterns, and the intricate

468 processes of the water cycle, and accurate numerical weather forecasting and climate

469 modeling (Charlesworth et al., 2023; Zheng et al., 2015; Li et al., 2016; Zhu et al.,

470 2023). In this investigation, the layered precipitable water (LPW) product obtained

471 from H8/9-AHI only provides clear-sky (refer to the flowchart in Figure 1) temperature

472 and humidity profiles and atmospheric instability indices. The next few satellite

473 products described in Sections 3.6 and 3.7 will also be processed only in clear-sky

474 pixels. The temperature and humidity profiles will be integrated into three distinct

475 layers for the output satellite product (High layer: from 700 to 300 hPa; Middle layer:

476 from 900 to 700 hPa; Low layer: from the surface to 900 hPa).

477 This physics-based LPW retrieval algorithm uses the BT observations at 6.2, 6.9, 7.3,

478 8.5, 10.4, 11.2, 12.3, and 13.3 μm channels to retrieve temperature and humidity

479 profiles. Since the temperature and humidity profiles can only be retrieved from clear-

480 sky pixels, we can express the forward IR radiative transfer equation observed by

481 satellite sensor as follows (Li et al., 2012; Li et al., 2000):

482 $$I_{obs}(\lambda) = \varepsilon_s(\lambda)B_s(\lambda)T_s(\lambda) - \int_0^{p_s} B(\lambda)dT(\lambda; 0, p) + [1 -$$

483 $$\varepsilon_s(\lambda)] \int_0^{p_s} B(\lambda)dT'(\lambda; 0, p), \qquad (11)$$

484 where T is the atmospheric transmittance above the pressure p. Subscript s signifies the

485 surface, $T' = T_s^2/T$. Similar to the OE method mentioned above, the cost function for

486 retrieving temperature and humidity profiles can be written as follows:

487 $$\zeta = [x - x_a]^T \gamma Cov_a^{-1}[x - x_a] + [y - M(x)]^T Cov_y^{-1}[y - M(x)], \qquad (12)$$

488 where the new added variable γ is the regularization parameter (or smoothing factor)

489 compared to Eq. (5). The introduction of the parameter γ aims to achieve faster

490 convergence and improve solution stability. The iterative 1DVAR algorithm can

491 increase or decrease parameter γ by determining the first-order variation of Eq. (11) (Li

492 et al., 2000). The first guessed temperature and humidity profiles for iterative retrieval

493 are obtained from spatial-temporally matched GFS-NWP data.

494   After retrieving the optimal temperature and humidity profiles, it will calculate five

495 atmospheric instability indices, including LI (Lifted Index), CAPE (Convective

496 Available Potential Energy), TT (Total Totals), KI (K Index), and SI (Showalter Index).

497 In weather forecasting, these indices can characterize the degree of development of

498 atmospheric instability features and provide the forecaster with a general idea of the

499 convective forcing. For instance, the LI represents the level of atmospheric

500 thermodynamic instability. A positive LI value indicates stability ($0 < LI$), while a

501 negative LI value suggests varying degrees of instability ($-3 < LI < 0$ marginally unstable,

502 $-6 < LI < -3$ moderately unstable, $-9 < LI < -6$ very unstable, and $LI < -9$ extremely unstable)

503 (Fernando et al., 2021). The valid ranges and usages of these five atmospheric

504 instability indices could refer to Table 1 and the study from Li et al., 2012. Note that,

505 considering the specific retrieval efficiency (processing LPW over the SCS region takes

506 approximately 20~25 minutes) of the H8/9-AHI LPW product, we have set the retrieval

507 frequency for LPW to 30 minutes.

508   Figure 7 presents a comparison between the LPW, encompassing total precipitable

509 water and water vapors at low, middle, and high layers, derived from the H9/AHI GEO

510 satellite and ERA5 reanalysis data at 09:00 UTC on January 4, 2023, specifically over

511 the SCS. The right column panel displays associated H9/AHI CAPE, K, LI, and

512 Showalter indices. Except for the water vapors at the high layer (700-300hPa), the

513 remaining LWP products exhibit negligible differences compared to the ERA5

514 reanalysis data in Figure 7.

515   To further validate the LPW products derived from H9/AHI, we conducted

516 comparisons against ERA5 reanalysis data for LPWs over a four-month period

517 mentioned above (January, April, July, and October of 2023). Figure 8 depicts the

518 comparison results for total precipitable water and LPWs at three distinct layers. The

519 correlation coefficients (R) for the LPWs at low, middle, and high layers, along with

520 total precipitable water, are respectively 0.919, 0.784, 0.725, and 0.876. These high

521 correlation coefficients indicate the relatively high quality of this product from the

522 NANO_SCS system.

523

524 *3.6 Land and sea surface temperatures*

525   Land and sea surface temperatures (LST and SST) are essential variables frequently
526   utilized in climate research community (Cai et al., 2022; Hong et al., 2022). In this
527   study, we incorporated a classical land surface temperature algorithm (Ulivieri and
528   Cannizzaro, 1985) into the NANO_SCS system, using split-windows channels of H8/9-
529   AHI (11.2 and 12.3 μm). This modified algorithm was also implemented as the
530   operational LST algorithm for the FY-4A GEO satellite (Dong et al., 2023) in China
531   Meteorological Administration (CMA), which can be easily expressed as follows:

532    $LST = C + A_1 BT_{11\mu m} + A_2(BT_{11\mu m} - BT_{12\mu m}) + A_3\varepsilon_s + D(BT_{11\mu m} -$
533        $BT_{12\mu m})(sec\theta - 1),$ (13)

534   where C, $A_{1\text{-}3}$, and D are the fitting coefficients, respectively. θ represents the satellite
535   zenith angle. ε_s is the surface emissivity. To account for the uncertainties in the LST
536   algorithm caused by water vapor, we conducted regression analysis using MODTRAN
537   V4.2 (Min et al., 2022; Berk et al., 2000; Dong et al., 2023) to derive fitting coefficients
538   for four distinct groups: daytime dry, daytime moist, nighttime dry, and nighttime moist
539   conditions. A threshold of water vapor content = 2.0 g/cm^2 was utilized to classify the
540   atmosphere as either dry or moist. This threshold value was obtained from matched
541   GFS-NWP data.

542   The classical and simplified Non-Linear Sea Surface Temperature (NLSST)
543   algorithm was used here to retrieve SST of H8/9-AHI (Walton et al., 1998), which is
544   expressed as follows:

545    $SST = a_0 + a_1 BT_{11\mu m} + a_2(BT_{11\mu m} - BT_{12\mu m}) + a_3(BT_{11\mu m} -$
546        $BT_{12\mu m})(sec\theta - 1),$ (14)

547   where $a_{0\text{-}3}$ are the fitting coefficients. The NOAA latest OISST (optimum interpolation
548   sea surface temperature) are used here to obtain fitting coefficients in Eq. (14) (Huang
549   et al., 2021; Reynolds et al., 2007). This global SST dataset, with a 0.25°×0.25°
550   horizontal resolution, covers the period from 1981 to the present.

551   Figure 9 shows the LST and SST comparisons between H9/AHI GEO satellite and
552   MODIS at 18:40 UTC on October 29, 2023. From this figure, we find consistent results
553   of LST and SST between our results and MODIS official products. Figures 9e and 9f
554   also shows the comparisons of the one year LST and SST from MODIS and H9/AHI
555   data over the SCS. The correlation coefficients (R) of these two products are about 0.96.
556
557   *3.7 Vegetation and water indices*

558   Vegetation and water indices, such as NDVI (Normalized Difference Vegetation
559   Index), NDSI (Normalized Differential Snow Index), NDWI (Normalized Differential
560   Water Index), and LSWI (Land Surface Water Index), are commonly utilized for
561   climate change, vegetation growth, urbanization, flood monitoring, etc. (Zheng et al.,
562   2021) (Hall et al., 1995) (Xiao et al., 2006) (Gu et al., 2007). In the NANO_SCS system,
563   these indices are calculated for clear-sky pixels during daytime using H8/9-AHI and
564   are expressed as follows:

565    $NDVI = (Ref_{0.86\mu m} - Ref_{0.64\mu m}) / (Ref_{0.86\mu m} + Ref_{0.64\mu m}),$ (15)

566    $NDSI = (Ref_{0.64\mu m} - Ref_{1.6\mu m}) / (Ref_{0.64\mu m} + Ref_{1.6\mu m}),$ (16)

567    $NDWI = (Ref_{0.86\mu m} - Ref_{2.23\mu m}) / (Ref_{0.86\mu m} + Ref_{2.23\mu m}),$ (17)

568    $LSWI = (Ref_{0.86\mu m} - Ref_{1.6\mu m}) / (Ref_{0.86\mu m} + Ref_{1.6\mu m}),$ (18)

569   where Ref represents the reflectance observed by satellite visible and near infrared
570   bands during the daytime. Unfortunately, in this study, the lack of a 0.47μm channel
571   prevents the computation of the Enhanced Vegetation Index (EVI). Figure 10 shows
572   the clear-sky NDVI, NDSI, NDWI, and LSWI maps from H9/AHI at 04:00 UTC on
573   December 1, 2023 over the SCS, which were generated by the NANO_SCS system.

574

575   **4. Data availability**

576   The Japanese Himawari-8 (H8) and Himawari-9 (H9) geostationary (GEO)
577   satellites are strategically positioned over the South China Sea (SCS), having been
578   launched on October 7, 2014, and November 2, 2016, respectively. It mainly provides
579   cloud mask, fraction, height, phase, optical and microphysical properties, layered
580   precipitable water, and sea surface temperature products, within a temporal resolution
581   of 10 minutes and a gridded resolution of 0.05° × 0.05°. Users can freely access sample
582   HDF-formatted files and data download instruction in PDF format of the South China
583   Sea datasets at https://doi.org/10.6084/m9.figshare.25015853 (Liu Jian, 2024). Besides,
584   for accessing related NRT satellite products, a quick-view website URL is provided:
585   [http://meteorsatellite.hellosea.org.cn/#/index]. Data can be download via FTP (File
586   Transfer Protocol) using the address FTP://www.hellosea.org.cn:10021, with the login
587   credentials being 'smlweix' and the password 'sml#456@'.

588

589   **5. Summary**

590   This investigation provides a comprehensive introduction to the key GEO satellite
591   science products generated by the NANO_SCS system and their evaluation. It offers

near-real-time atmospheric and oceanic science products of Himawari-8/9 geostationary satellites over the South China Sea from November 13, 2022, to the present. Positioned at 140.7°E and 0° latitude, the H8/9 geostationary satellites mainly cover East Asia, Oceania, and the Indian Ocean. The standard NRT Level-2 satellite science products encompass the region between 0° to 40°N latitude and 100°E to 140°E longitude with a grid resolution of $0.05° \times 0.05°$ and a 10-minute interval (except for LPW products, retrieved every 30 minutes). These products are derived from 14 spectral channels with a 4km horizontal resolution.

The NANO_SCS system provides a range of atmospheric and oceanic products, including cloud mask, fraction, height, phase, optical and microphysical properties, layered precipitable water, land surface temperature, sea surface temperature, and more. These near-real-time satellite products were rigorously evaluated against independent datasets, including MODIS satellite-based products and ERA5 reanalysis data. The results highlight strong consistency between NRT H8/9 geostationary satellite atmospheric and oceanic science products and the reference data from similar sensors and ERA5 over the South China Sea.

Future continuation of atmospheric and oceanic science products generated by the NANO_SCS system is also operated and secured by the Southern Marine Science and Engineering Guangdong Laboratory (Zhuhai) in China. Preparations are underway for new products such as atmospheric motion vectors (AMV) and quantitative precipitation estimates (QPE) in near-real-time production. Besides, the qualities of current GEO satellite products will be further validated and enhanced. Chinese FY-4C GEO satellite, scheduled for launch in 2025 or 2026, will offer higher spatial resolution and additional channels, including an IR hyperspectral sounder, to further extend and improve the NANO_SCS-system-based data records for atmospheric and oceanic parameters.

Author contributions. JL and MM contributed to designing the research; MM, JL, and WW implemented the research and wrote the original draft; JL supervised the research; all co-authors revised the paper and contributed to the writing.

628

646

647

648

649

650

651

652

653

654

655

References

Baum, B. A., P. Yang, S. Nasiri, A. J. Heidinger, A. Heymsfield, and J. Li: Bulk scattering properties from the remote sensing of ice clouds. Part III: High resolution spectral models from 100 to 3250 cm-1, Journal of Applied Meteorology and Climatology, *46*, 423 - 434, doi:10.1175/JAM2473.1, 2007.

Bennartz, R.: Global assessment of marine boundary layer cloud droplet number concentration from satellite, Journal of Geophysical Research - Atmospheres, *112*, D02201, doi:10.1029/2006JD007547, 2007.

Berk, A., G. P. Anderson, P. K. Acharya, J. H. Chetwynd, L. S. Bernstein, E. P. Shettle, M. W. Matthew, and S. M. Adler-Golden (2000), MODTRAN4 user's manual, edited, Air Force Research Laboratory.

Bessho, K., et al.: An introduction to Himawari-8/9—Japan's new-generation geostationary meteorological satellites, Journal of the Meteorological Society of Japan, *94*, 151-183, doi:10.2151/jmsj.2016-009, 2016.

Cai, W., B. Ng, G. Wang, A. Santoso, L. Wu, and K. Yang: Increased ENSO sea surface temperature variability under four IPCC emission scenarios, Nature Climate Change, *12*, 228–231, 2022.

Charlesworth, E., et al.: Stratospheric water vapor affecting atmospheric circulation, Nature Communications, *14*, 3925, doi:10.1038/s41467-023-39559-2, 2023.

Chou, M.-D., M. J. Suarez, C.-H. Ho, M. M.-H. Yan, and K.-T. Lee: Parameterizations for cloud overlapping and shortwave single-scattering properties for use in general circulation and cloud ensemble models, J Climate, *11*, 202-214, doi:10.1175/1520-0442(1998)011<0202:PFCOAS>2.0.CO;2, 1998.

Ding, Y., and Y. Liu: Onset and the evolution of the Summer Monsoon over the South China Sea during SCSMEX Field Experiment in 1998, Journal of the Meteorological Society of Japan, *V79*, 255-276, doi:10.2151/jmsj.79.255, 2001.

Dong, L., S. Tang, F. Wang, M. Cosh, X. Li, and M. Min: Inversion and validation of FY-4A official land surface temperature product, Remote Sensing, *15*, 2437, doi:10.3390/rs15092437 2023.

Fernando, M., Millangoda, M., and Premalal, S.: Analyze and Comparison of the Atmospheric Instability Using K-Index, Lifted Index Total Totals Index Convective Availability Potential Energy (CAPE) and Convective Inhibition (CIN) in Development of Thunderstorms in Sri Lanka During Second Inter-Monsoon, Multi-Hazard Early Warning and Disaster Risks, Cham, 2021//, 603-614,

Gu, Y., Brown, J. F., Verdin, J. P., and Wardlow, B. D.: A five-year analysis of MODIS NDVI and NDWI for grassland drought assessment over the central Great Plains of the United States, Geophysical Research Letters, 34, 2007.

Hall, D. K., Riggs, G. A., and Salomonson, V. V.: Development of methods for mapping global snow cover using moderate resolution imaging spectroradiometer data, Remote Sensing of Environment, 54, 127-140, 1995.

Heidinger, A., and M. Pavolonis: Gazing at cirrus clouds for 25 years through a split window, part 1: Methodology, Journal of Applied Meteorology and Climatology, *48*, 1110-1116, doi:10.1175/2008JAMC1882.1, 2009.

Heidinger, A. K., A. T. Evan, M. J. Foster, and A. Walther: A naive Bayesian cloud-

detection scheme derived from CALIPSO and applied within PATMOS-x, Journal of Applied Meteorology and Climatology, *51*, 1129–1144, doi:10.1175/JAMC-D-11-02.1, 2012.

Hersbach, H., et al.: The ERA5 global reanalysis, Quarterly Journal of the Royal Meteorological Society, *146*, 1999–2049, doi:10.1002/qj.3803, 2020.

Heymsfield, A. J., S. Matrosov, and B. Baum: Ice water path-optical depth relationships for cirrus and deep stratiform ice cloud layers, J Appl Meteorol, *42*, 1369–1390, doi:10.1175/1520-0450(2003)042<1369:IWPDRF>2.0.CO;2, 2007.

Hong, F., W. Zhan, F.-M. Göttsche, Z. Liu, P. Dong, H. Fu, F. Huang, and X. Zhang: A global dataset of spatiotemporally seamless daily mean land surface temperatures: generation, validation, and analysis, Earth System Science Data, *14*, 3091–3113, doi:10.5194/essd-14-3091-2022, 2022.

Huang, B., C. Liu, V. Banzon, E. Freeman, G. Graham, B. Hankins, T. Smith, and H.-M. Zhang: Improvements of the Daily Optimum Interpolation Sea Surface Temperature (DOISST) Version 2.1, J Climate, *34*, 2923-2939, doi:10.1175/JCLI-D-20-0166.1, 2021.

Husi, L., T. M. Nagao, T. Y. Nakajima, J. Riedi, H. Ishimoto, A. J. Baran, H. Shang, M. Sekiguchi, and M. Kikuchi: Ice cloud properties from Himawari-8/AHI next-generation geostationary satellite: Capability of the AHI to monitor the DC cloud generation process, IEEE Transactions on Geoscience and Remote Sensing, *57*, 3229-3239, doi:10.1109/TGRS.2018.2882803 2019.

Jiang, J., T. Zhou, Y. Qian, C. Li, F. Song, H. Li, X. Chen, W. Zhang, and Z. Chen: Precipitation regime changes in High Mountain Asia driven by cleaner air, Nature, doi:10.1038/s41586-023-06619-y, 2023.

Kim, D., M. Gu, T.-H. Oh, E.-K. Kim, and H.-J. Yang: Introduction of the advanced meteorological imager of Geo-Kompsat-2a: In-orbit tests and performance validation, Remote Sensing, *13*, 1303, doi:10.3390/rs13071303, 2021.

King, M. D., S. C. Tsay, S. E. Planick, M. Wang, and K. N. Liou: Cloud retrieval algorithms: Optical thickness, effective particle radius, and thermodynamic phase, NASA MODIS Algorithm Theoretical Basis Documents, 1997.

Koseki, S., K. Tieh-Yong, and T. Chee-Kiat: Effects of the cold tongue in the South China Sea on the monsoon, diurnal cycle and rainfall in the Maritime Continent, Quarterly Journal of the Royal Meteorological Society, *139*, 1566-1582, doi:10.1002/qj.2052, 2013.

Lai, R., S. Teng, B. Yi, H. Letu, M. Min, S. Tang, and C. Liu: Comparison of cloud properties from Himawari-8 and FengYun-4A geostationary satellite radiometers with MODIS cloud retrievals, Remote Sensing, *11*, 1703, doi:10.3390/rs11141703, 2019.

Letu, H., T. M. Nagao, T. Y. Nakajima, J. Riedi, H. Ishimoto, A. J. Baran, H. Shang, M. Sekiguchi, and M. Kikuchi: Ice cloud properties from Himawari-8/AHI next-generation geostationary satellite: Capability of the AHI to monitor the DC cloud generation process, IEEE Transactions on Geoscience and Remote Sensing, *57*, 3229-3239, doi:10.1109/tgrs.2018.2882803, 2019.

Letu, H., et al.: High-resolution retrieval of cloud microphysical properties and surface solar radiation using Himawari-8/AHI next-generation geostationary satellite, Remote Sensing of Environment, *239*, 111583, doi:10.1016/j.rse.2019.111583, 2020.

Levenberg, K.: A method for the solution of certain non-linear problems in least squares, Quarterly of Applied Mathematics, *2*, 164-168, 1944.

Li, J., W. P. Menzel, T. J. Schmit, and J. Schmetz: Applications of geostationary hyperspectral infrared sounder observations – progress, challenges, and future perspectives, Bulletin of the American Meteorological Society, doi:10.1175/BAMS-D-21-0328.1, 2022a.

Li, J., T. J. Schmit, X. Jin, and G. Martin: GOES-R Advanced Baseline Imager (ABI) Algorithm Theoretical Basis Document For Legacy Atmospheric Moisture Profile, Legacy Atmospheric Temperature Profile, Total Precipitable Water, and Derived Atmospheric Stability Indices NOAA Goes-R ATBD, 109, 2012.

Li, J., P. Wang, H. Han, J. Li, and J. Zheng: On the assimilation of satellite sounder data in cloudy skies in numerical weather prediction models, Journal of Meteorological Research, *30*, 169–182, 2016.

Li, J., W. W. Wolf, W. P. Menzel, W. Zhang, H.-L. Huang, and T. H. Achtor: Global soundings of the atmosphere from ATOVS measurements: The algorithm and validation, Journal of Applied Meteorology, *39*, 1248–1268, doi:10.1175/1520-0450(2000)039<1248:GSOTAF>2.0.CO;2, 2000.

Li, Y., G. Ren, Q. Wang, L. Mu, and Q. Niu: Marine heatwaves in the South China Sea: Tempo-spatial pattern and its association with large-scale circulation, Remote Sensing, *14*, 5829, doi:10.3390/rs14225829, 2022b.

Liang, Y., M. Min, Y. Yu, X. Wang, and P. Xia: Assessing diurnal cycle of cloud covers of Fengyun-4A geostationary satellite based on the manual observation data in China, IEEE Transactions on Geoscience and Remote Sensing, *61*, doi:10.1109/TGRS.2023.3256365, 2023.

Liu, B., Y. Liu, G. Wu, J. Yan, J. He, and S. Ren: Asian summer monsoon onset barrier and its formation mechanism, Climate Dynamics, *45*, 711–726, doi:10.1007/s00382-014-2296-0, 2014.

Liu Jian, Y. J., Lin Chuyong, He Min, Liu Haiyan, Min Min, Wang Wei (2024), Near real-time atmospheric and oceanic science products of Himawari-8/9 geostationary satellites over the South China Sea, edited, figshare. Dataset., doi:https://doi.org/10.6084/m9.figshare.25015853.

Ma, Z., J. Li, W. Han, Z. Li, Q. Zeng, W. P. Menzel, T. J. Schmit, D. Di, and C.-Y. Liu: Four‑dimensional wind fields from geostationary hyperspectral infrared sounder radiance measurements with high temporal resolution, Geophys Res Lett, *48*, e2021GL093794, doi:10.1029/2021GL093794, 2021.

Martin, D. W., and M. R. Howland: Rainfall over the Arabian Sea during the onset of the 1979 monsoon, Nature, *300*, 628–630, 1982.

Min, M., et al.: Estimating summertime precipitation from Himawari-8 and global forecast system based on machine learning, IEEE Transactions on Geoscience

and Remote Sensing, *57*, 2557-2570, doi:10.1109/TGRS.2018.2874950, 2019.

Min, M., B. Chen, N. Xu, X. He, X. Wei, and M. Wang: Nonnegligible diurnal and long-term variation characteristics of the calibration biases in Fengyun-4A/AGRI infrared channels based on the oceanic drifter data, IEEE Transactions on Geoscience and Remote Sensing, *60*, 1-15, doi:10.1109/TGRS.2022.3160450, 2022.

Min, M., J. Deng, C. Liu, N. Lu, X. Hu, L. Chen, J. Guo, P. Zhang, Q. Lu, and L. Wang: An investigation of the implications of lunar illumination spectral changes for Day/Night Band based cloud property retrieval due to lunar phase transition, Journal of Geophysical Research: Atmospheres, *122*, 9233-9244, doi:10.1002/2017JD027117, 2017a.

Min, M., J. Li, F. Wang, Z. Liu, and W. P. Menzel: Retrieval of cloud top properties from advanced geostationary satellite imager measurements based on machine learning algorithms, Remote Sensing of Environment, *239*, 111616, doi:10.1016/j.rse.2019.111616 2020.

Min, M., et al.: Developing the science product algorithm testbed for Chinese next-generation geostationary meteorological satellites: Fengyun-4 series, Journal of Meteorological Research, *31*, 708-719, doi:10.1007/s13351-017-6161-z, 2017b.

Mülmenstädt, J., M. Salzmann, J. E. Kay, M. D. Zelinka, P.-L. Ma, C. Nam, J. Kretzschmar, S. Hörnig, and J. Quaas: An underestimated negative cloud feedback from cloud lifetime changes, Nature Climate Change, *11*, 508–513, doi:10.1038/s41558-021-01038-1, 2021.

Nakajima, T., and M. D. King: Determination of the optical thickness and effective particle radius of clouds from reflected solar radiation measurements. Part I: Theory, J Atmos Sci, *48*, 728-750, 1990.

Niu, Q., and Y. Feng: Relationships between the typhoon-induced wind and waves in the northern South China Sea, Geophys Res Lett, *48*, e2020GL091665, doi:10.1029/2020GL091665, 2021.

Noh, Y.-J., J. M. Forsythe, S. D. Miller, C. J. Seaman, Y. Li, A. K. Heidinger, D. T. Lindsey, M. A. Rogers, and P. T. Partain: Cloud-base height estimation from VIIRS. Part II: A statistical algorithm based on A-Train satellite data, Journal of Atmospheric and Oceanic Technology, *34*, 585–598, doi:10.1175/JTECH-D-16-0110.1, 2017.

Parol, F., J. C. Buriez, G. Brogniez, and Y. Fouquart: Information content of AVHRR channels 4 and 5 with respect to the effective radius of cirrus cloud particles, J Appl Meteorol, *30*, 973–984, 1991.

Pavolonis, M.: GOES-R Advanced Baseline Imager (ABI) Algorithm Theoretical Basis Document For Cloud Type and Cloud Phase Version 2.0, NOAA GOES-R ATBD, 1-96, 2010a.

Pavolonis, M. J.: Advances in extracting cloud composition information from spaceborne infrared radiances-A robust alternative to brightness temperatures. Part I: Theory, Journal of Applied Meteorological Climatology, *49*, 1992-2012, 2010b.

830 Pavolonis, M. J., A. K. Heidinger, and T. Uttal: Daytime global cloud typing from
831   AVHRR and VIIRS: Algorithm description, validation, and comparisons J Appl
832   Meteorol, *44*, 804-826, 2005.

833 Platnick, S., M. D. King, S. A. Ackerman, W. P. Menzel, B. A. Baum, J. C. Riédi, and
834   R. A. Frey: The MODIS cloud products: Algorithms and examples from Terra,
835   IEEE Transactions on Geoscience and Remote Sensing, *41*, 459-473,
836   doi:10.1109/TGRS.2002.808301, 2003.

837 Platnick, S., et al.: The MODIS cloud optical and microphysical products: Collection 6
838   updates and examples from Terra and Aqua, IEEE Transactions On Geoscience
839   and Remote Sensing, *55*, 502-525, doi:10.1109/TGRS.2016.2610522, 2017.

840 Reynolds, R., T. M. Smith, C. Liu, D. Chelton, K. Casey, and M. Schlax: Daily high-
841   resolution-blended analyses for sea surface temperature, J Climate, *20*, 5473-
842   5496, doi:10.1175/2007JCLI1824.1, 2007.

843 Rodgers, C. D.: Inverse methods for atmospheric sounding: Theory and practice, 2000.

844 Schmit, T. J., P. Griffith, M. M. Gunshor, J. M. Daniels, S. J. Goodman, and W. J. Lebair:
845   A closer look at the ABI on the GOES-R Series Bulletin of the American
846   Meteorological Society, *98*, 681-698 doi:10.1175/BAMS-D-15-00230.1, 2017.

847 Soldi, G., et al.: Space-based global maritime surveillance. Part I: Satellite technologies,
848   IEEE Aerospace and Electronic Systems Magazine *36*, 8-28,
849   doi:10.1109/MAES.2021.3070862, 2021.

850 Ulivieri, C., and G. Cannizzaro: Land surface temperature retrievals from satellite
851   measurements, Acta Astronaut, *12*, 985–997, doi:10.1016/0094-
852   5765(85)90026-8, 1985.

853 Viúdez-Mora, A., C.-S. M., J. Calbó, and J. A. González: Modeling atmospheric
854   longwave radiation at the surface during overcast skies: The role of cloud base
855   height, Journal of Geophysical Research: Atmospheres, *120*, 199-214,
856   doi:10.1002/2014JD022310, 2015.

857 Walther, A., W. Straka, and A. K. Heidinger: GOES-R Advanced Baseline Imager (ABI)
858   algorithm theoretical basis document for daytime cloud optical and
859   microphysical properties (DCOMP), NOAA Goes-R ATBD, 2011.

860 Walton, C. C., W. G. Pichel, J. F. Sapper, and D. A. May: The development and
861   operational application of nonlinear algorithms for the measurement of sea
862   surface temperatures with the NOAA polar-orbiting environmental satellites,
863   Journal of Geophysical Research, *103*, 27999-28012, doi:10.1029/98JC02370,
864   1998.

865 Wang, B., F. Huang, Z. Wu, J. Yang, X. Fu, and K. Kikuchi: Multi-scale climate
866   variability of the South China Sea monsoon: A review, Dynamics of
867   Atmospheres and Oceans, *47*, 15-37, doi:10.1016/j.dynatmoce.2008.09.004,
868   2009.

869 Wang, F., M. Min, N. Xu, C. Liu, Z. Wang, and L. Zhu: Effects of linear calibration
870   errors at low temperature end of thermal infrared band: Lesson from failures in
871   cloud top property retrieval of FengYun-4A geostationary satellite, IEEE
872   Transactions on Geoscience and Remote Sensing, *60*, 5001511,

doi:10.1109/TGRS.2022.3140348, 2022.

Wang, G., S.-P. Xie, T. Qu, and R. X. Huang: Deep South China Sea circulation, Geophys Res Lett, *38*, L05601, doi:10.1029/2010GL046626, 2011.

Wang, M., M. Min, J. Li, B. Chen, H. Lin, Z. Yao, N. Xu, and M. Zhang: Applicability of physics-based and machine-learning-based algorithms of geostationary satellite in retrieving the diurnal cycle of cloud base height, Atmospheric Chemistry and Physics Discussion, 2024.

Wang, X., Q.-Y. Liu, D. Sui, and D. Wang: The imprint of the ENSO activities on the South China Sea wave climate, Ocean Dynamics, *70*, 1315–1323, doi:10.1007/s10236-020-01400-5, 2020.

Wang, X., M. Min, F. Wang, J. Guo, B. Li, and S. Tang: Intercomparisons of cloud mask product among Fengyun-4A, Himawari-8 and MODIS, IEEE Transactions on Geoscience and Remote Sensing, *57*, 8827-8839, doi:10.1109/TGRS.2019.2923247 2019.

Whitaker, J. S., T. M. Hamill, X. Wei, Y. Song, and Z. Toth: Ensemble data assimilation with the NCEP global forecast system, Monthly Weather Review, *136*, 463–482, doi:10.1175/2007MWR2018.1, 2008.

Xia, P., M. Min, Y. Yu, Y. Wang, and L. Zhang: Developing a near real-time cloud cover retrieval algorithm using geostationary satellite observations for photovoltaic plants, Remote Sensing, *15*, 1141, doi:10.3390/rs15041141, 2023.

Xia, P., L. Zhang, M. Min, J. Li, Y. Wang, Y. Yu, and S. Jia: Accurate nowcasting on cloud cover at solar photovoltaic plants using geostationary satellite images, Nature Communications, *15*, 1-10, doi:10.1038/s41467-023-44666-1, 2024.

Xiao, X., Boles, S., Frolking, S., Li, C., Babu, J. Y., Salas, W., and Moore, B.: Mapping paddy rice agriculture in South and Southeast Asia using multi-temporal MODIS images, Remote Sensing of Environment, *100*, 95-113, https://doi.org/10.1016/j.rse.2005.10.004, 2006.

Xu, W., S. A. Rutledge, and K. Chudler: Diurnal cycle of coastal convection in the South China Sea region and modulation by the BSISO*34*, 4297–4314, doi:10.1175/JCLI-D-20-0308.1, 2021.

Yang, J., Z. Zhang, C. Wei, F. Lu, and Q. Guo: Introducing the new generation of Chinese geostationary weather satellites, FengYun-4, Bulletin of the American Meteorological Society, *98*, 1637-1658, doi:10.1175/BAMS-D-16-0065.1, 2017.

Zhao, G., and L. D. Girolamo: Cloud fraction errors for trade wind cumuli from EOS-Terra instruments, Geophys Res Lett, *33*, L20802, doi:10.1029/2006GL027088, 2006.

Zheng, J., J. Li, T. J. Schmit, J. Li, and Z. Liu: The impact of AIRS atmospheric temperature and moisture profiles on hurricane forecasts: Ike (2008) and Irene (2011), Advances in Atmospheric Sciences, *32*, 319–335, 2015.

Zheng, Y., L. Tang, and H. Wang: An improved approach for monitoring urban built-up areas by combining NPP-VIIRS nighttime light, NDVI, NDWI, and NDBI, Journal of Cleaner Production, *328*, 129488, doi:10.1016/j.jclepro.2021.129488,

916   2021.

917 Zhou, R., X. Pan, Z. Xiaohu, X. Na, and M. Min: Research progress and prospects of
918   atmospheric motion vector based on meteorological satelliteimages, Reviews of
919   Geophysics and Planetary Physics (In Chinese), *55*, 184-194,
920   doi:10.19975/j.dqyxx.2022-077, 2024.

921 Zhu, L., R. Zhou, D. Di, W. Bai, and Z. Liu: Retrieval of atmospheric water vapor
922   content in the rnvironment from AHI/H8 using both physical and random forest
923   methods—A case study for typhoon Maria (201808), Remote Sensing, *15*, 498,
924   doi:10.3390/rs15020498, 2023.

925
926

927

928

929

930

931

932

933

934

935

936

937

938

939

940

941

942

943

944

945

Tables and Figures

Table 1. Primary NRT H8/9 GEO satellite atmospheric and oceanic science products

and related variables generated by the NANO_SCS system.

Product Name (Abbr.)	Variable Name	Valid Value	Unit	Note
Cloud Mask (CLM)	Cloud_Mask	0=Cloudy; 1=Probably cloudy; 2=Probably clear ; 3=Clear	None	
Cloud Fraction (CLF)	Cloud_Fraction	0-100	%	down-sampled 5×5 pixel box
Cloud Type and Phase (CLP)	Cloud_Type	0=Clear; 1=Spare; 2=Liquid water; 3=Supercooled water; 4=Mixed; 5=Optically thick ice; 6=Optically thin ice; 7=Multilayered ice; 8=Uncertainty	None	
	Cloud_Phase	0=Clear; 1=Liquid water; 2=Supercooled water; 3=Mixed; 4=Ice; 5=Uncertainty	None	
Cloud Top Properties (CTP)	Cloud_Top_Height	0-30000	m	
	Cloud_Top_Pressure	0-2000	hPa	
	Cloud_Top_Temperature	0-400	K	
	Cloud_Emissivity_at_11µm	0-100	%	
Cloud Optical and Microphysical Properties (COT)	Cloud_Optical_Depth	0-150	None	only daytime
	Cloud_Effective_Radius	0-100	µm	only daytime
	Cloud_Liquid_Water_Path	0-1000	g/m^2	only daytime
	Cloud_Ice_Water_Path	0-1000	g/m^2	only daytime
Cloud Base Properties (CBP)	Cloud_Base_Height	0-30000	m	only daytime
	Cloud_Base_Pressure	0-2000	hPa	only daytime
Sea Surface Temperature (SST)	Sea_Surface_Temperature	0-400	K	
Land Surface Temperature (LST)	Land_Surface_Temperature	0-400	K	
Vegetation/Water Indices (NDI)	NDVI (Normalized Difference Vegetation Index)	0-1.0	None	only daytime
	NDSI (Normalized Differential Snow Index)	0-1.0	None	only daytime
	NDWI (Normalized Differential Water Index)	0-1.0	None	only daytime
	LSWI (Land Surface Water Index)	0-1.0	None	only daytime
Layered Precipitable Water (LPW)	Total_Precipitable_Water	0-1000	mm	
	Water_Vapor_High	0-1000	mm	700-300hPa
	Water_Vapor_Middle	0-1000	mm	900-700hPa
	Water_Vapor_Low	0-1000	mm	Surface-900hPa
	CAPE_Index (Convective Available Potential Energy)	0-10000	J/kg	
	K_Index	-100-100	K	
	LI_Index (Lifted)	0-400	K	Stored in Celsius
	Showalter_Index	0-400	K	Stored in Celsius
	TT_Index (Total totals)	0-400	K	Stored in Celsius

949

950

951

952
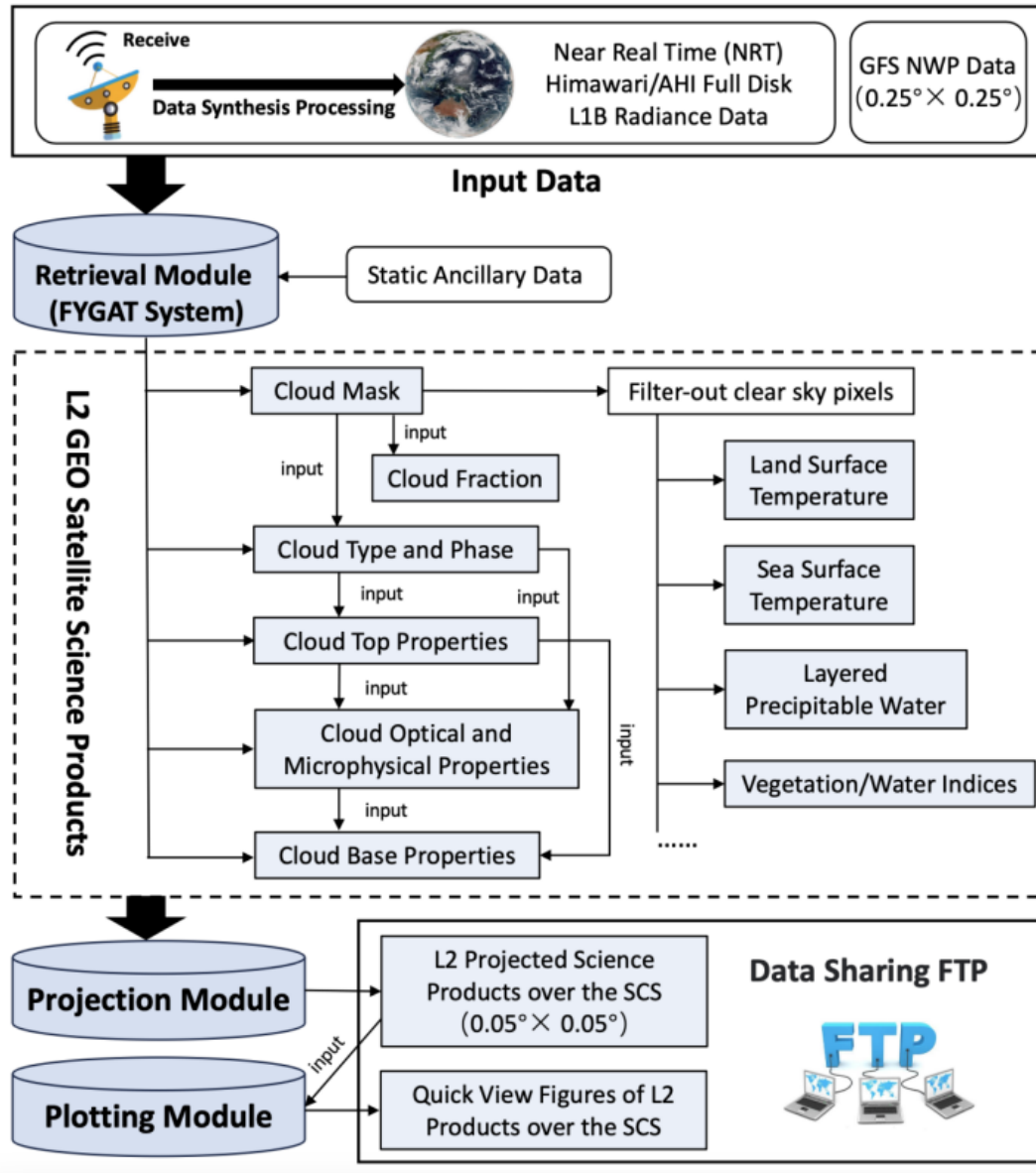
Figure 1. Flowchart of the NANO_SCS system. Dark gray shading represents key processing module; light gray shading represents satellite science product.
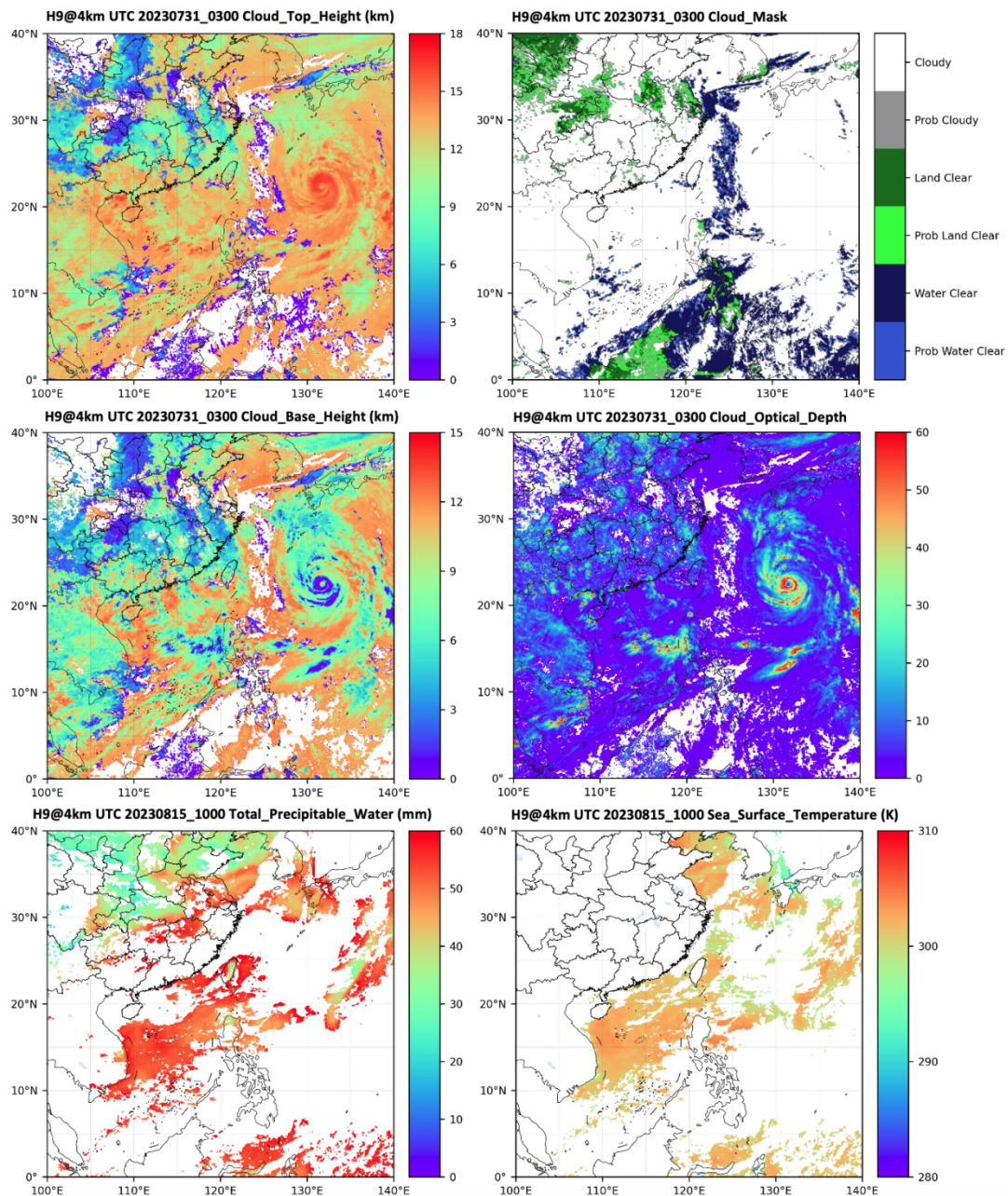
956

957

958

959

960

961

962

Figure 2. H9/AHI GEO satellite cloud top height (left top panel), cloud mask (right top panel), cloud base height (left middle panel), cloud optical depth (right middle panel) at 03:00 UTC on July 31, 2023, and atmospheric total precipitable water (left bottom panel) and sea surface temperature (right bottom panel) at 10:00 UTC on August 15, 2023 over the NANO_SCS system.

969

970
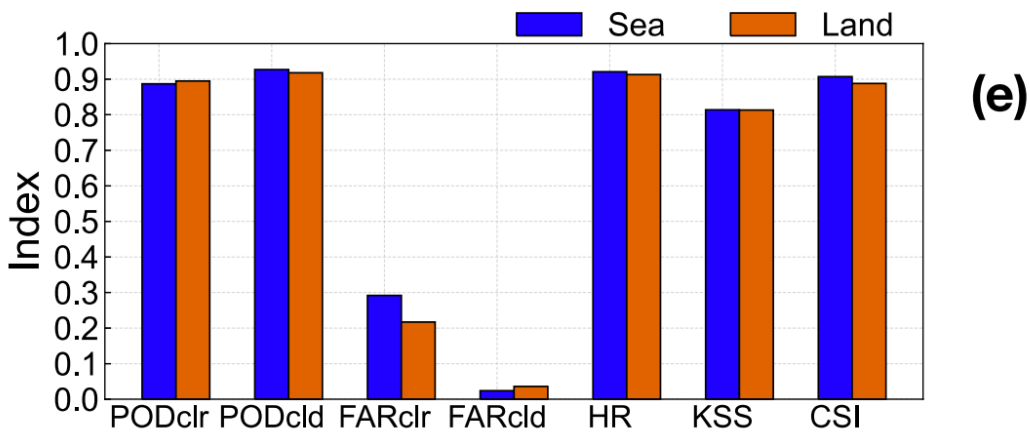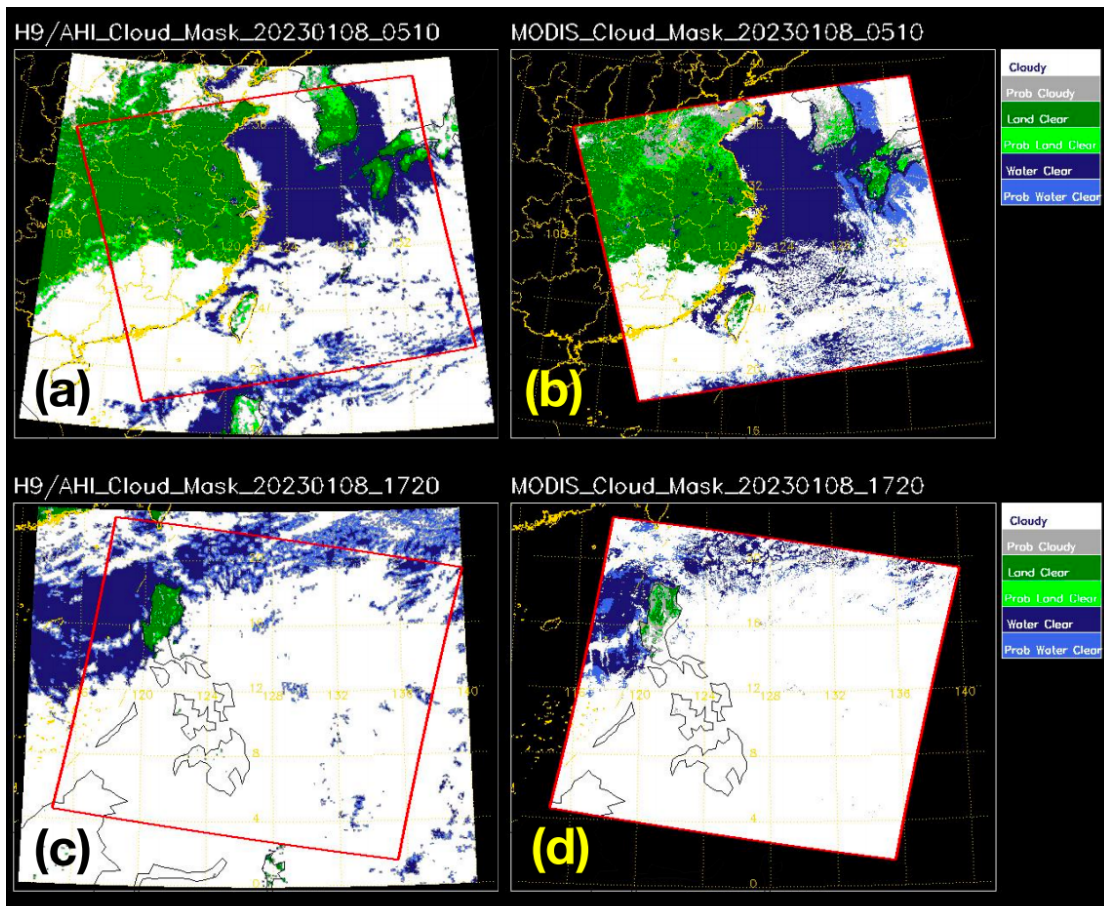
971

Figure 3. Cloud mask comparisons between (a, c) H9/AHI GEO satellite and (b, d) MODIS at 05:10 (top panel) and 17:20 (middle panel) UTC on January 8, 2023. (e) POD, FAR, HR, and KSS scores of H9/AHI results for all the matched pixels over land (earthy yellow) and sea (blue) in January, April, July, and October of 2023. "clr" and "cld" respectively signify the clear-sky and cloudy-sky pixels.

982
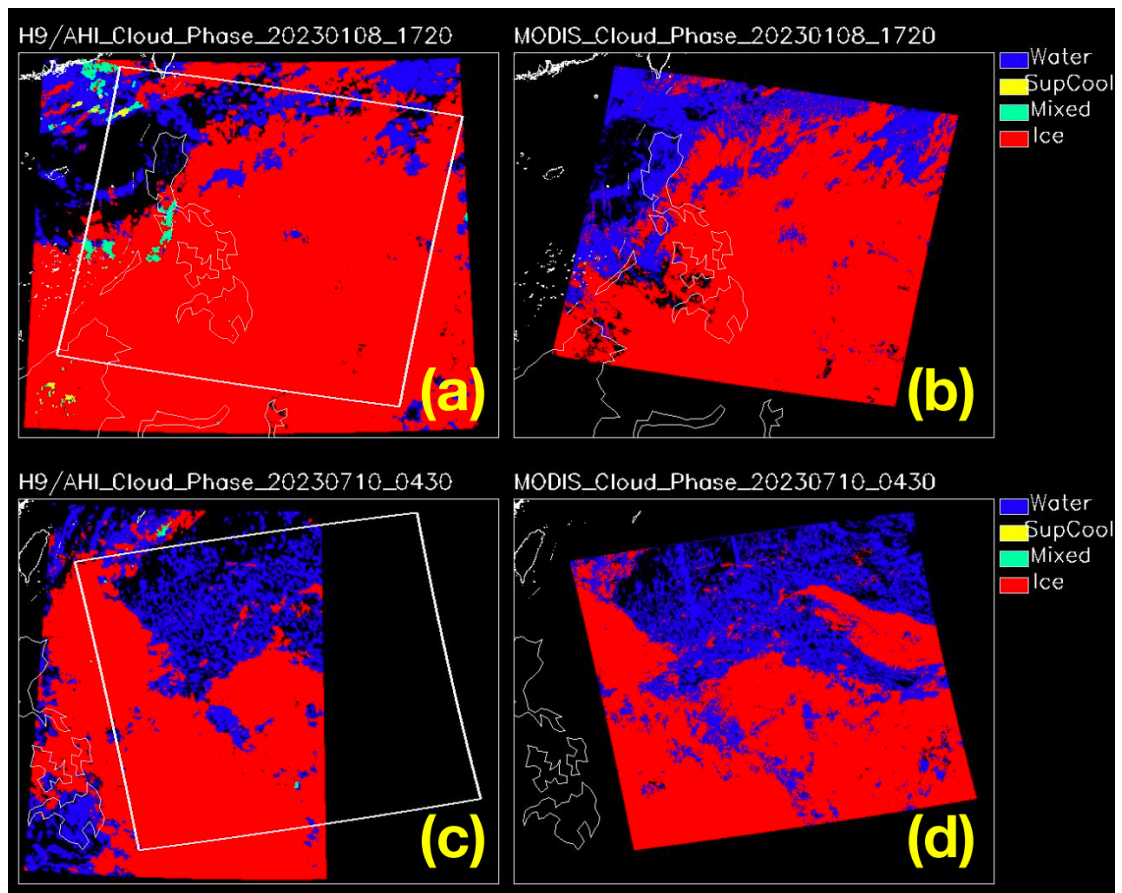
Figure 4. Cloud phase comparisons between (a, c) H9/AHI GEO satellite and (b, d) MODIS at 05:10 UTC (top panel) on January 8, 2023 and 04:30 UTC (bottom panel) on July 10, 2023.

987

988

989

990

991

992

993

994

995

996

997

998

999

1000

1001
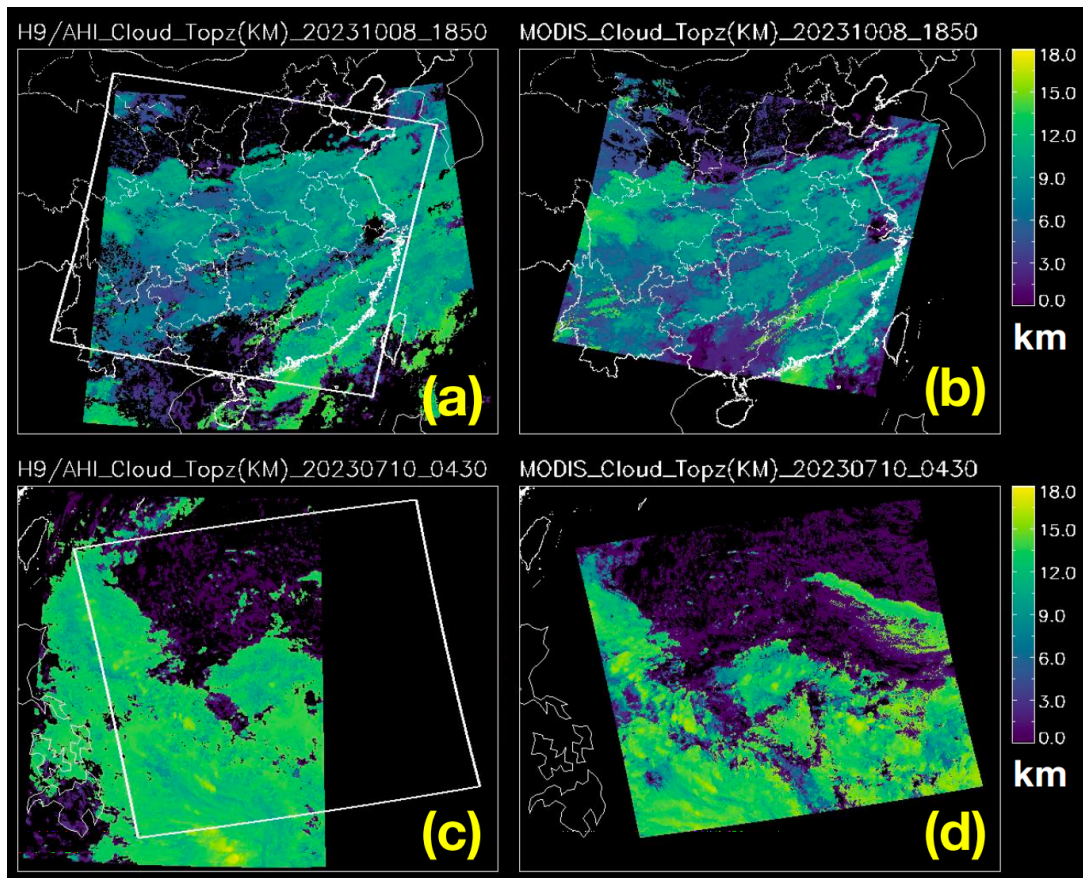
Figure 5. Cloud top height comparisons between (a, c) H9/AHI GEO satellite and (b,
d) MODIS at 18:50 UTC (top panel) on October 8, 2023 and 04:30 UTC (bottom panel)
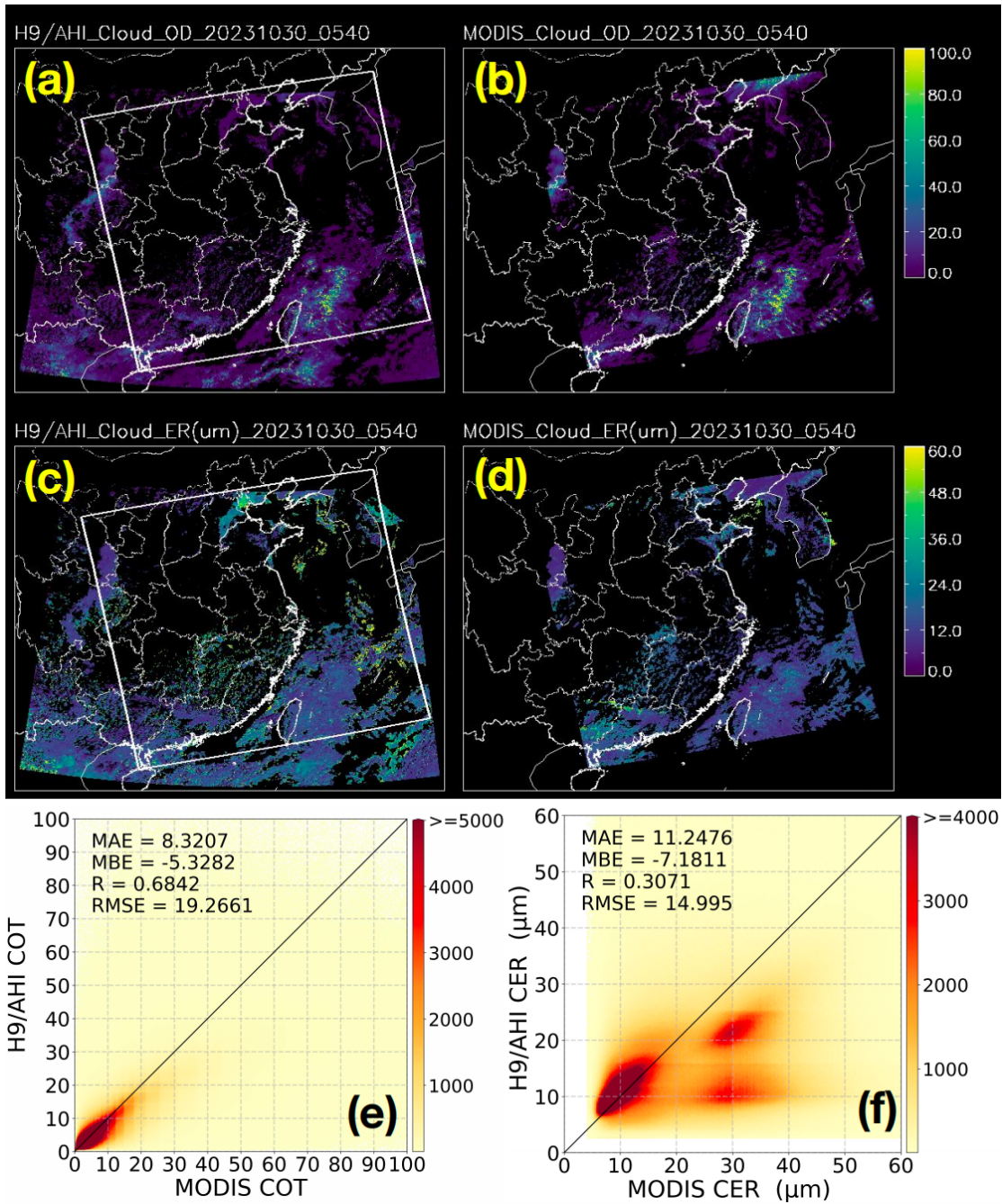on July 10, 2023.

1002

1003

1004

1005

1006

1007

1008

1009

1010

1011

1012

1013

1014

1015

1016

1017

1018

1019

1020

1021 **Figure 6.** Cloud optical depth (top panel) and effective radius (middle panel)

1022 comparisons between (a, c) H9/AHI GEO satellite and (b, d) MODIS at 05:40 UTC on

1023 October 30, 2023. Comparisons of the one year (2023) (e) cloud optical depth and (f)

1024 effective radius from MODIS and H9/AHI data over the NANO_SCS system. The color

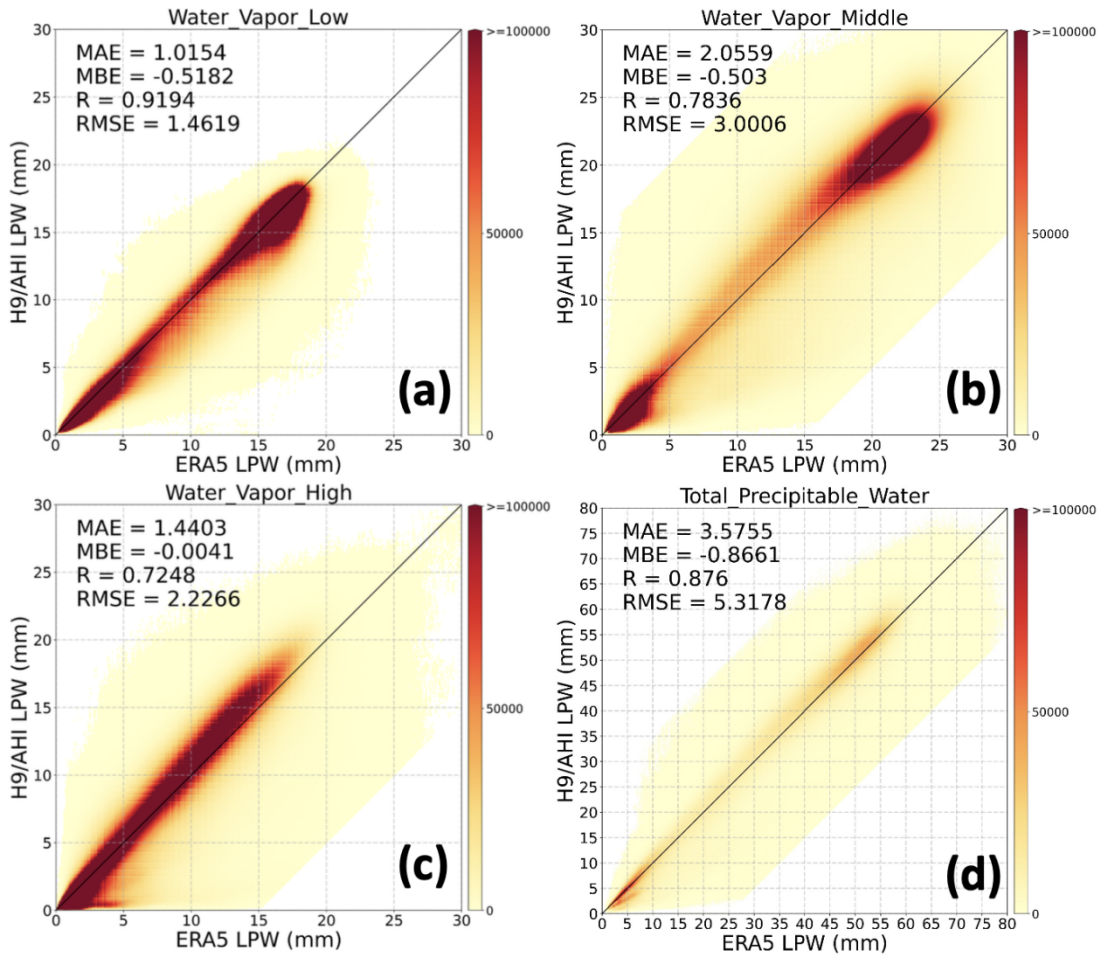1025 bar represents the total number in every bin at an interval of 0.2 of COT or 0.2 μm of

1026 CER.

1027

1028
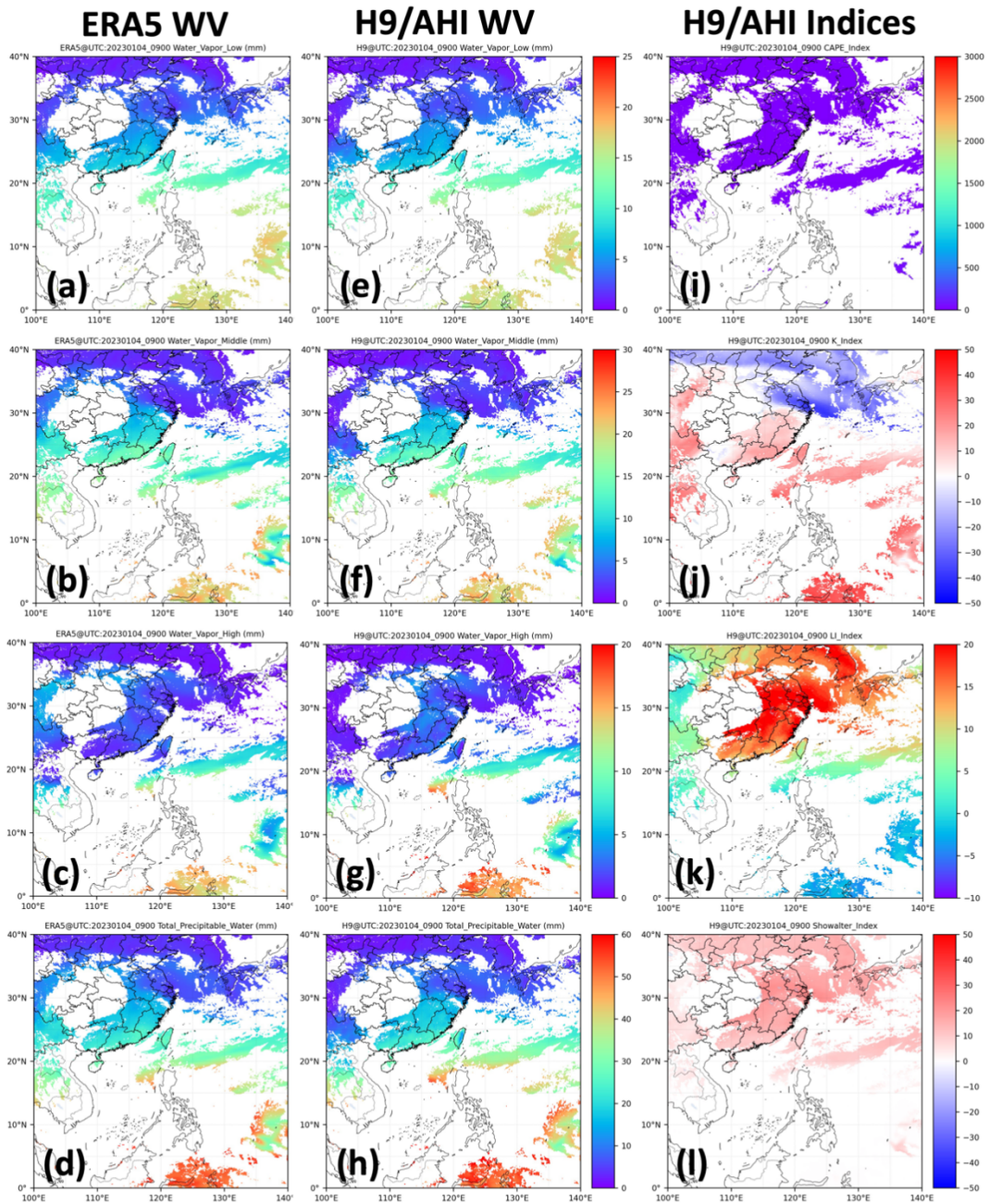
1029

Figure 7. ERA5 (first column panel) and H9/AHI GEO satellite (middle column panel) atmospheric (a, e) water vapor at low layer (Surface-900hPa), (b, f) water vapor at middle layer (900-700hPa), (c, g) water vapor at high layer (700-300hPa), (d, h) total precipitable water, (i) H9/AHI CAPE index, (j) H9/AHI K index, (k) H9/AHI LI index, and (l) H9/AHI Showalter index at 09:00 UTC on January 4, 2023 over the NANO_SCS system.

1036

1037

Figure 8. Comparisons of the one year (2023) layered precipitable water (LPW) values (a, Low; b, Middle; c, High; d, Total) from ERA5 reanalysis and H9/AHI data over the NANO_SCS system. The color bar represents the total number in every bin at an interval of 0.1 mm.
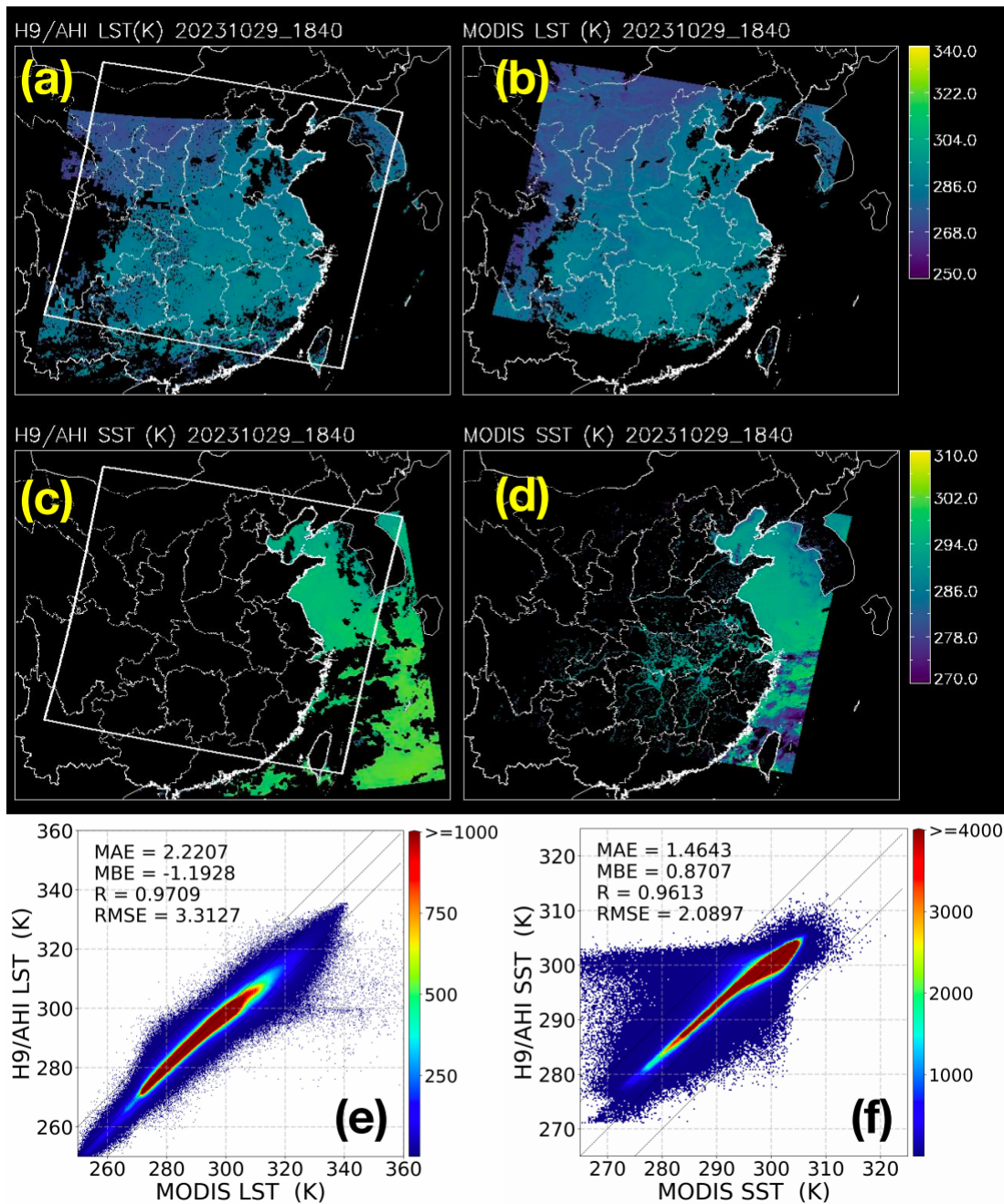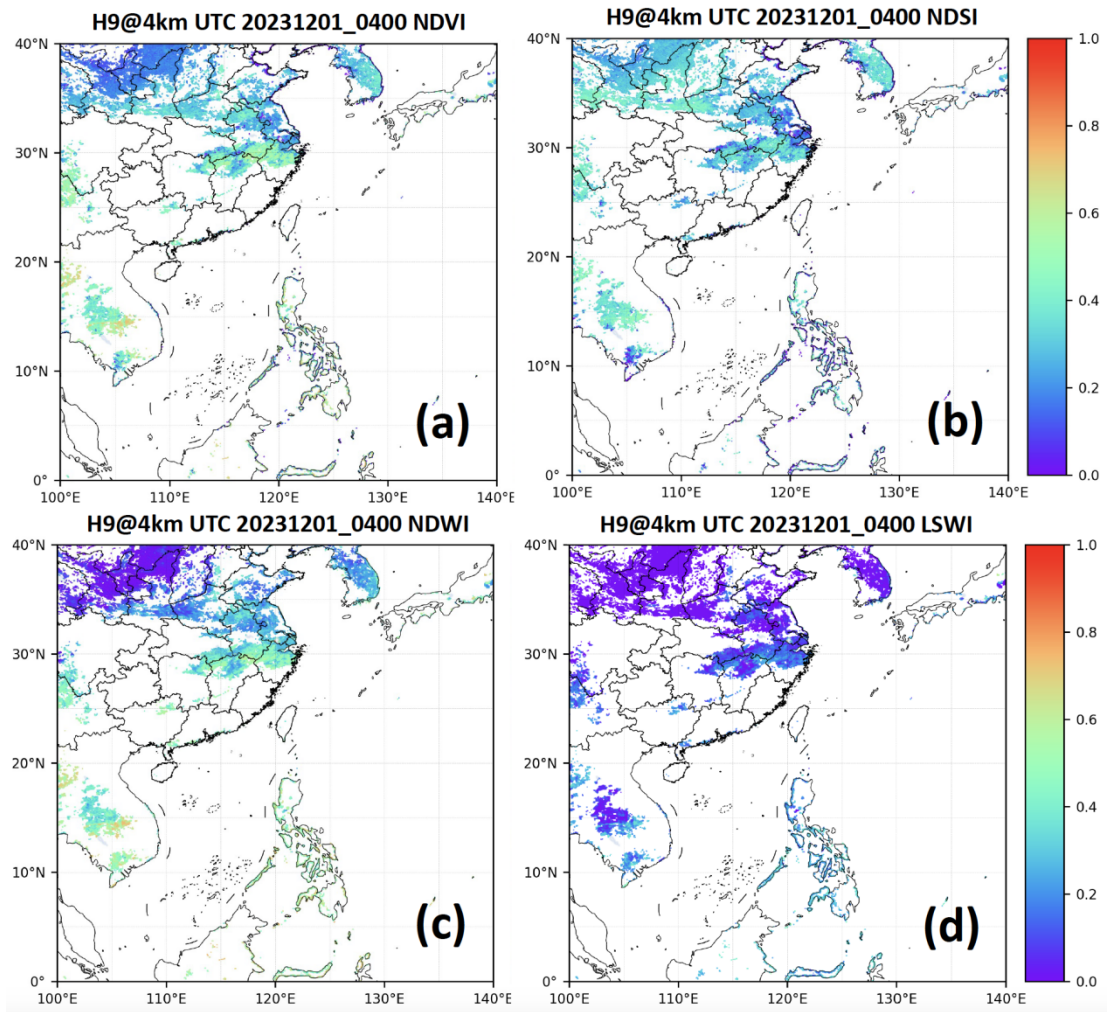
1056

Figure 9. LST (top panel) and SST (middle panel) comparisons between (a, c) H9/AHI GEO satellite and (b, d) MODIS at 18:40 UTC on October 29, 2023. Comparisons of the one year (2023) (e) LST and (f) SST from MODIS and H9/AHI data over the NANO_SCS system. The color bar represents the total number in every bin at an interval of 0.25 K of LST or SST.

1062

1063

1064

1065

1066

1067 **Figure 10.** (a) NDVI, (b) NDSI, (c) NDWI, and (d) LSWI maps retrieved by H9/AHI

1068 at 04:00 UTC on December 1, 2023 over the NANO_SCS system.

1069